A Sommerfeld non-reflecting boundary condition for the wave equation in mixed form

Hector Espinoza [a], Ramon Codina [a,*], Santiago Badia [a,b]

[a] *Universitat Politècnica de Catalunya, Jordi Girona 1-3, Edifici C1, E-08034 Barcelona, Spain*
[b] *Centre Internacional de Mètodes Numèrics en Enginyeria, Parc Mediterrani de la Tecnologia, Esteve Terradas 5, E-08860 Castelldefels, Spain*

Abstract

In this paper we develop numerical approximations of the wave equation in mixed form supplemented with non-reflecting boundary conditions (NRBCs) of Sommerfeld-type on artificial boundaries for truncated domains. We consider three different variational forms for this problem, depending on the functional space for the solution, in particular, in what refers to the regularity required on artificial boundaries. Then, stabilized finite element methods that can mimic these three functional settings are described. Stability and convergence analyses of these stabilized formulations including the NRBC are presented. Additionally, numerical convergence test are evaluated for various polynomial interpolations, stabilization methods and variational forms. Finally, several benchmark problems are solved to determine the accuracy of these methods in 2D and 3D.
© 2014 Elsevier B.V. All rights reserved.

1. Introduction

Many engineering problems dealing with waves involve infinite domains. Usually, the infinite domain is truncated for computational purposes and the wave problem is solved in a finite domain [1,2]. Non-reflecting boundaries (NRBs) have to be considered, which must allow the waves to leave the truncated domain avoiding

* Corresponding author. Tel.: +34 934016486.
  E-mail addresses: hector.espinoza@upc.edu (H. Espinoza), ramon.codina@upc.edu (R. Codina), sbadia@cimne.upc.edu (S. Badia).
  URLs: https://www.upc.edu/espinoza (H. Espinoza), http://www.codina.rmee.upc.edu (R. Codina), http://www.badia.rmee.upc.edu (S. Badia).

spurious reflections that may pollute the solution in the interior of the computational domain of interest. There are many types of NRBs, which can be classified into two groups, namely, non-reflecting boundary conditions (NRBCs) and non-reflecting boundary layers (NRBLs). NRBCs are boundary conditions on the artificial boundary that absorb impinging waves. On the other hand, NRBLs have the property of absorbing waves that are traveling inside the layer.

NRBL techniques have been applied to the time-domain wave equation in irreducible [3,4] and mixed form [5,6], and to the linearized Euler equations [7–9]. Perhaps the most popular among the NRBL techniques is the Perfectly Matched Layer (PML). The PML concept was developed by Berenger in 1994 for electromagnetic scattering [10]. The idea is to add an absorbing layer to the domain designed to have zero reflection for any plane wave and to make the solution decay exponentially inside the layer [11].

A classical example of NRBC is the so-called Sommerfeld boundary (or radiation) condition [12]. It relates the temporal derivative and the normal derivative of the unknown in the case of boundaries far away from sources and normal to the propagating wave. Thus, it is inexact for non-perpendicular wave incidence and boundaries close to sources, and therefore it has to be understood as an approximate boundary condition to avoid wave reflection in these cases. NRBCs have also been applied to the time-domain wave equation in irreducible [13–16] and mixed form [17], as well as for the linearized Euler equations in [18,17].

The error $\mathcal{E}$ introduced by a NRBC is the difference between the exact solution in the unbounded domain and the solution in the truncated domain with the artificial boundary. Let J be the order of the NRBC, R the distance of the artificial boundary to the wave source, k_t the tangential wave number and ω the wave angular frequency. The error $\mathcal{E}$ introduced by a NRBC of order J [2] behaves as

$$\mathcal{E} = \mathcal{O}\left(\frac{k_t^2}{\omega^2}\right)^J = \mathcal{O}\left(\frac{1}{R^2}\right)^J. \tag{1}$$

For a fixed location of the artificial boundary, increasing the order J reduces the error introduced by the NRBC. If the error approaches zero as J increases the NRBC is exact, whereas if the error does not approach zero the NRBC is asymptotic [1].

Many NRBCs have been developed and can be classified as classical, exact non-local and local high-order. Among classical NRBCs we have those proposed by Engquist–Majda [19], Bayliss–Turkel [20] and Higdon [21]. Classical NRBCs appeared as an improvement of Sommerfeld NRBC and can be high-order in theory, but in practice only low-order versions are used because of the presence of high-order derivatives which are difficult to handle numerically [11]. Among exact non-local NRBCs we have Dirichlet-to-Neumann formulations [22] and the Difference Potential Method [23]. Exact non-local NRBCs involve a boundary integral operator which couples all the points on the boundary [11]. Among local high-order NRBCs we have those due to Collino [24], Grote–Keller [25], Rowley–Colonius [26], Guddati–Tassoulas [27], Givoli–Neta [16] and Hagstrom–Warburton [28]. Local high-order NRBCs are high-order in theory and can be implemented up to any desired order in practice, which can be achieved introducing auxiliary variables [11].

The wave equations can be posed in irreducible form, leading to a second-order (in space and time) scalar partial differential equation. Many applications require the vector-valued unknown of the problem, which can be computed by the solution of the irreducible form plus a post-processing step, but leads to a poor approximation of it. In order to improve the convergence rate for the vector field, we can consider the problem as a first-order (in space and time) hyperbolic system, that involves both the scalar and vector unknowns. The wave equation in mixed form is in fact mandatory for some applications in solid mechanics or in nonlinear waves in shallow waters.

The finite element (FE) approximation in space of this hyperbolic problem is not straightforward, since its well-posedness relies on an inf–sup condition. Thus, Galerkin FE schemes require mixed interpolations that satisfy a discrete version of this compatibility condition [29]. Inf–sup stable FE formulations have been developed for several mixed problems, e.g., [30] for the Stokes problem, [31] for the Darcy problem, [32] for the Maxwell problem, [33,34] for the Stokes–Darcy problem, [35] for the wave equation, and [36,37] for elastodynamics. As an alternative to inf–sup stable formulations, we can consider stabilized FE formulations [38]. Stabilized FEs add new terms to the Galerkin formulation, which provide the required stability for well-posedness (without the need to rely on a discrete inf–sup condition) keeping optimal convergence properties. This

way, we are able to use equal interpolation for the scalar and vector unknowns of the wave equation in mixed form.

In this work, we develop novel stabilized FE formulations for wave scattering problems on unbounded domains truncated via Sommerfeld-type boundary conditions as the simplest example of NRBC. Our starting point is the formulation recently presented and analyzed in [39]. It is a stabilized FE method with the important feature of allowing for different functional settings. This is accomplished by *transferring* regularity from the scalar to the vector unknowns or vice versa [39] through an appropriate integration by parts and design of the stabilization parameters. Summarizing, the main contributions of the article are:

- Statement of the mixed form of the wave equation with Sommerfeld artificial boundary conditions in three different functional settings. It is an extension of the work in [39], in which the functional setting has to be properly modified in order to give sense to the Sommerfeld terms; extra regularity is required on the artificial boundary for the vector unknown. One of the resulting formulations has already been proposed in [17], whereas the other two problem settings are new. We observe that the new functional spaces are in fact complete.
- Extension of the stabilized FE formulations in [39] to deal with Sommerfeld boundary conditions. We design stabilized FE formulations that can mimic the three functional settings proposed at the continuous level. Stability and convergence results are presented, and their proof is sketched. A set of numerical experiments is performed to check the convergence of the formulations, as well as the error introduced by the Sommerfeld boundary condition.

The organization of the paper is as follows. In Section 2, we present the wave equation in irreducible and mixed form and in time and frequency domain. Additionally, we describe the Sommerfeld boundary condition applied to the wave equation. We also propose three different functional settings for the time-domain wave problem in mixed form truncated with Sommerfeld boundary conditions. In Section 3, we describe the spatial discretization we propose, which is a stabilized FE method (in two different versions), and show how to mimic the three functional settings by properly integrating by parts and choosing the stabilization parameters. Section 4 is devoted to the stability and convergence analysis of these formulations, respectively. In all these sections, time is left continuous, concentrating the exposition only in the spatial approximation. In Section 5 we carry out convergence tests and evaluate the performance of the NRBC through various benchmark problems in 2D and 3D. Finally, we draw some conclusions in Section 6.

2. Problem statement

In this section, we state the wave equation in mixed form in time and frequency domain. Further, we state the Sommerfeld artificial boundary conditions in both cases. The use of Sommerfeld-type boundary conditions for the mixed form of the wave equation has been used in [17] (without using this terminology). Waves are commonly found in many physical phenomena such as acoustic and electromagnetic scattering, fluid dynamics, and elastodynamics. To fix ideas, we will use the terminology of waves propagating in fluids, although our approach is obviously general.

2.1. Wave equation in time and frequency domain

Waves can be described in time domain or frequency domain. In both cases, the problem involves a spatial domain $\Omega \subset \mathbb{R}^d$, where d is the space dimension ($d = 1, 2, 3$). Let Γ be its boundary and $\boldsymbol{x} \in \Omega$ any spatial point. From hereafter, we will refer to vectors in $\mathbb{R}^d$ simply as vectors. Further, we use the following convention: lower-case bold italic letters represent vectors in $\mathbb{R}^d$, and non-bold letters represent scalars. Both complex and real numbers are used in this section. We implicitly assume real numbers unless otherwise specified.

In the time domain, the problem is posed in $\Xi := \Omega \times \Upsilon$, where $t \in \Upsilon := (0, T)$ denotes a time value. The long term behavior, i.e. $T \to \infty$, will not be considered in this work. The time-domain wave equation in its irreducible form reads as:

$$\frac{1}{c^2}\partial_{tt}p' - \Delta p' = f', \tag{2}$$

where $p'(\boldsymbol{x}, t)$ is the unknown (real-valued scalar function), f' is a forcing term and c is the wave speed. Alternatively, we can consider the wave equation in mixed form:

$$\mu_p \partial_t p' + \nabla \cdot \boldsymbol{u}' = f_p, \tag{3}$$

$$\mu_u \partial_t \boldsymbol{u}' + \nabla p' = \boldsymbol{f}_u, \tag{4}$$

where the unknowns $p'(\boldsymbol{x}, t)$ and $\boldsymbol{u}'(\boldsymbol{x}, t)$ are real-valued scalar and vector functions, respectively, $\mu_p > 0$ and $\mu_u > 0$ are the physical parameters of the equation and $[f_p, \boldsymbol{f}_u]$ are forcing terms. The coefficients μ_p and μ_u that characterize the mixed wave equation (3) and (4) are related to the wave speed c appearing in irreducible form of the scalar wave equation (2) as follows:

$$c^2 = (\mu_p \mu_u)^{-1}.$$

Time domain analysis solves the wave problem for the full range of frequencies involved. The only limit for the frequencies captured at time-discrete level is the size of the time step used for the time discretization. Frequency domain analysis results from a Fourier transform in time of the time-domain problem and solves the wave problem for one angular frequency ω. In the irreducible case, it leads to the scalar Helmholtz equation:

$$\Delta \hat{p} + k^2 \hat{p} = \hat{f}_k, \tag{5}$$

where $\hat{p}(\boldsymbol{x})$ is now the unknown (complex-valued scalar function), and $k = \omega/c$ is the wavenumber corresponding to a certain angular frequency ω. As in the time domain case, we can also make use of the Helmholtz equation in mixed form:

$$-\mathrm{i}\mu_p \omega \hat{p} + \nabla \cdot \hat{\boldsymbol{u}} = \hat{f}_p, \tag{6}$$

$$-\mathrm{i}\mu_u \omega \hat{\boldsymbol{u}} + \nabla \hat{p} = \hat{\boldsymbol{f}}_u, \tag{7}$$

where $\hat{p}(\boldsymbol{x})$ and $\hat{\boldsymbol{u}}(\boldsymbol{x})$ are complex unknowns, ω is the angular frequency, $\hat{f}_p$ and $\hat{\boldsymbol{f}}_u$ are forcing terms and $\mathrm{i} = \sqrt{-1}$.

Notice that the number of unknowns in the wave equation in mixed form (both in the time and frequency domain) is $d + 1$ times the ones in irreducible form, but the regularity requirements in space and time can be made less stringent for p'. In all cases, the wave equation has to be supplemented with appropriate initial and boundary conditions. In the case of the mixed form, boundary conditions also depend on the functional setting of the problem.

2.2. Sommerfeld boundary condition

The Sommerfeld boundary condition is a type of NRBC, that takes its name from the German theoretical physicist Arnold Sommerfeld, applicable when the sources are concentrated in a region of the space and the exterior boundary is a sphere surrounding it and centered at the source region. Additionally, the spherical surface has to be far away from the source, so that one can assume that the impinging waves only have radial component when they reach the artificial boundary. In spherical coordinates and for the scalar Helmholtz equation in 3D (frequency domain), the Sommerfeld radiation condition can be expressed as:

$$\lim_{r \to \infty} \left(r(\partial_r \hat{p} - \mathrm{i}k\hat{p}) \right) = 0,$$

where r is radial component in the spherical coordinate system and ∂_r is the derivative in the radial direction.[1] In spherical coordinates and for the scalar wave equation in irreducible form in 3D (time domain) the Sommerfeld radiation condition can be written as:

---

[1] Some authors write the Sommerfeld radiation condition with a + sign, but that depends on the time variation assumption. In this work, we have assumed a harmonic time variation with harmonics of the form $\mathrm{e}^{-\mathrm{i}\omega t}$, which gives the minus sign.

$$\lim_{r \to \infty} \left(r \left(\partial_r p' + \frac{1}{c} \partial_t p' \right) \right) = 0.$$

On the other hand, when considering the mixed form of these equations, the Sommerfeld radiation condition can be written in two different ways:

$$\lim_{r \to \infty} \left(r \left(\sqrt{\mu_p} \partial_r p' - \sqrt{\mu_u} \nabla \cdot \boldsymbol{u}' \right) \right) = 0,$$
$$\lim_{r \to \infty} \left(r \left(\sqrt{\mu_p} \partial_t p' - \sqrt{\mu_u} \partial_t u_r' \right) \right) = 0. \tag{8}$$

In the frequency domain, these Sommerfeld boundary conditions lead to:

$$\lim_{r \to \infty} \left(r \left(\sqrt{\mu_p} \partial_r \hat{p} - \sqrt{\mu_u} \nabla \cdot \hat{\boldsymbol{u}} \right) \right) = 0,$$
$$\lim_{r \to \infty} \left(r \left(\sqrt{\mu_p} \hat{p} - \sqrt{\mu_u} \hat{u}_r \right) \right) = 0.$$

Condition (8) can be simplified taking out the temporal derivative, which yields

$$\lim_{r \to \infty} \left(r \left(\sqrt{\mu_p} p' - \sqrt{\mu_u} u_r' + C(\boldsymbol{x}) \right) \right) = 0.$$

$C(\boldsymbol{x})$ is a time-independent function defined on Γ, which can be determined from initial conditions. Assuming that $\sqrt{\mu_p} p'(\boldsymbol{x}, 0) - \sqrt{\mu_u} u_r'(\boldsymbol{x}, 0) = 0$ holds on the artificial boundary, we get $C(\boldsymbol{x}) = 0$. It leads to the final expression

$$\lim_{r \to \infty} \left(r \left(\sqrt{\mu_p} p' - \sqrt{\mu_u} u_r' \right) \right) = 0.$$

This Sommerfeld radiation condition is a limit for $r \to \infty$, and establishes a fast decay of $\sqrt{\mu_p} p' - \sqrt{\mu_u} u_r'$. If $R < \infty$, the *approximation* that we may consider is $\sqrt{\mu_p}\, p' - \sqrt{\mu_u} u_r' = 0$ at $r = R$. Moreover, if the boundary is not a sphere, we may replace u_r' by $\boldsymbol{n} \cdot \boldsymbol{u}'$, $\boldsymbol{n}$ being the unit normal exterior to the boundary. Thus, we may consider the approximation

$$\sqrt{\mu_p} p' - \sqrt{\mu_u} \boldsymbol{n} \cdot \boldsymbol{u}' = 0. \tag{9}$$

Because of its simplicity, this is the boundary condition we propose to enforce on the artificial boundary for the mixed wave equation in time domain. In the following sections, we show that this boundary condition has good non-reflecting properties and is stable, in spite of having been superseded in accuracy by high order NRBCs. The analysis of its performance in combination with the FE method we propose is the subject of this paper.

2.3. Initial and boundary value problem

Let us split Γ into three disjoint sets denoted as Γ_p, Γ_u and Γ_o. The scalar unknown p is enforced on Γ_p, the normal trace of the vector unknown $\gamma_n \boldsymbol{u}$ on Γ_u (γ_n denotes the normal trace operator), and the NRBC we wish to analyze on Γ_o (the artificial boundary). The problem consists in finding $p : \Xi \longrightarrow \mathbb{R}$ and $\boldsymbol{u} : \Xi \longrightarrow \mathbb{R}^d$ such that:

$$\mu_p \partial_t p + \nabla \cdot \boldsymbol{u} = f_p, \tag{10}$$

$$\mu_u \partial_t \boldsymbol{u} + \nabla p = \boldsymbol{f}_u \tag{11}$$

with the initial conditions

$$p(\boldsymbol{x}, 0) = 0, \quad \boldsymbol{u}(\boldsymbol{x}, 0) = \boldsymbol{0} \tag{12}$$

and with the boundary conditions

$$p = 0 \text{ on } \Gamma_p, \quad \gamma_n \boldsymbol{u} := \boldsymbol{n} \cdot \boldsymbol{u} = 0 \text{ on } \Gamma_u, \quad \mu_p^{1/2} p = \mu_u^{1/2} \gamma_n \boldsymbol{u} \text{ on } \Gamma_o. \tag{13}$$

Let us define two auxiliary variables denoted as κ_p and κ_u defined as:

$$\kappa_p := \left(\frac{\mu_p}{\mu_u}\right)^{1/2}, \quad \kappa_u := \left(\frac{\mu_u}{\mu_p}\right)^{1/2}.$$

Let Ψ be a generic spatial domain, i.e., Ω or Γ or part of them. Let $L^2(\Psi)$ be the space of square integrable functions defined on Ψ, and $L^2(\Psi)^d$ the space of vector functions with components in $L^2(\Psi)$. $H^1(\Psi)$ is the space of functions in $L^2(\Psi)$ with derivatives in $L^2(\Psi)$, $H(\text{div}, \Psi)$ the space of vector functions with components and divergence in $L^2(\Psi)$. Any of the spaces defined previously will be denoted generically as X. Additionally, for an arbitrary functional space X, its norm will be denoted as $\|\cdot\|_X$. In the case of $L^2(\Omega)$ or $L^2(\Omega)^d$, the L^2-norm will simply be denoted as $\|\cdot\|$ and the L^2-inner-product as $(\cdot,\cdot)$. Furthermore, the space of functions whose X-norm is C^r continuous in the time interval Υ will be denoted by $C^r(\Upsilon; X)$. (We will only be interested in the cases $r = 0$ and $r = 1$.) Functions whose X-norm is L^p in Υ will be denoted by $L^p(\Upsilon; X)$.

Furthermore, let V_p, V_u be the functional spaces associated with p and $\boldsymbol{u}$, respectively. These spaces will be defined afterwards because they depend on the functional setting. Additionally, let us define $V := V_p \times V_u$ and $L := L^2(\Omega) \times L^2(\Omega)^d$.

Problem (10) and (11) with appropriate initial and boundary conditions will be stated for

$$p \in C^1(\Upsilon; L^2(\Omega)) \cap C^0(\Upsilon; V_p),$$
$$\boldsymbol{u} \in C^1(\Upsilon; L^2(\Omega)^d) \cap C^0(\Upsilon; V_u)$$

with f_p and $\boldsymbol{f}_u$ in regular enough spaces.

2.4. Internal energy and power flux

Let us multiply (10) against p, (11) against $\boldsymbol{u}$, add the resulting equations and integrate over Ω. Applying the divergence theorem, we get the energy balance equation:

$$\frac{1}{2}\mu_p \frac{\mathrm{d}}{\mathrm{d}t}\|p\|^2 + \frac{1}{2}\mu_u \frac{\mathrm{d}}{\mathrm{d}t}\|\boldsymbol{u}\|^2 = -\int_\Gamma \boldsymbol{n} \cdot p\boldsymbol{u} \, \mathrm{d}\Gamma + (f_p, p) + (\boldsymbol{f}_u, \boldsymbol{u}).$$

The *total internal energy* E is defined as:

$$E := \frac{1}{2}\left(\mu_p\|p\|^2 + \mu_u\|\boldsymbol{u}\|^2\right),$$

which contains the *potential energy* $\frac{1}{2}\mu_p\|p\|^2$ and the *kinetic energy* $\frac{1}{2}\mu_u\|\boldsymbol{u}\|^2$. The energy per unit time, i.e. the power added through the boundary, is defined as:

$$P_b := -\int_\Gamma \boldsymbol{n} \cdot p\boldsymbol{u} \, \mathrm{d}\Gamma,$$

whereas the power of the external forces is defined as:

$$P_f := (f_p, p) + (\boldsymbol{f}_u, \boldsymbol{u}).$$

The power flux (energy per unit time per unit surface) at any given point of the boundary is $\boldsymbol{n} \cdot p\boldsymbol{u}$. The Sommerfeld boundary condition prescribed on Γ_o is the one that ensures that energy always flows out of the boundary because $\boldsymbol{n} \cdot p\boldsymbol{u} \geqslant 0$ everywhere at any instant of time, i.e., $P_b \leqslant 0$. It makes the problem well-posed, since the solution is bounded by the data. With these definitions we can write the energy balance equation as:

$$\frac{\mathrm{d}E}{\mathrm{d}t} = P_b + P_f. \tag{14}$$

Our interest in Eq. (14) relies in the fact that it represents the power balance of the system and it reveals the interaction of the forces and boundaries with the domain.

2.5. Variational problem

The variational form of problem (10)–(13) can be expressed in three different ways. Each one requires a certain regularity on the unknowns p and $\boldsymbol{u}$, which amounts to say that p and $\boldsymbol{u}$ should belong to a particular space of functions. In all cases the problem reads: find $[p, \boldsymbol{u}] \in C^1(\Upsilon; L) \cap C^0(\Upsilon; V)$ such that

$$\mathcal{B}([p, \boldsymbol{u}], [q, \boldsymbol{v}]) = \mathcal{L}([q, \boldsymbol{v}]) \tag{15}$$

for all test functions $[q, \boldsymbol{v}] \in V$ and the respective initial conditions. The bilinear form $\mathcal{B}$, the linear form $\mathcal{L}$ and the space V are defined in three different ways depending on the variational form into consideration. For simplicity, we will assume that the forcing terms f_p and $\boldsymbol{f}_u$ are square integrable, although we could relax this regularity requirement and assume they belong to the dual space of V_p and V_u, respectively.

The three different variational formulations of problem (10)–(13) essentially differ in the way integration-by-parts from the strong form of the problem is performed and in the regularity required for the unknowns. In the problem statement given below, variational form I (16)–(20) is obtained without integrating by parts any term. Thus, boundary conditions on both scalar and vector quantities have to be imposed strongly. Pressures in $H^1(\Omega)$ have well-defined traces in $L^2(\Gamma)$, and the pressure boundary condition on Γ_p has sense. The velocity space $H(\text{div}, \Omega)$ does not have a continuous γ_n operator onto $L^2(\Gamma)$. Thus, in order for the Sommerfeld condition $p = \kappa_u \gamma_n u$ to have sense in $L^2(\Omega)$ (which is required for $p \in H^1(\Omega)$), we consider a more regular velocity space, viz., the space of $H(\text{div}, \Omega)$ with normal traces in $L^2(\Omega)$. We can easily check that the resulting bilinear/linear forms in (16) and (17) are continuous in this functional setting.

Variational form I

$$V_p = \{q \in H^1(\Omega) \mid q = 0 \text{ on } \Gamma_p\},$$
$$V_u = \{\boldsymbol{v} \in H(\text{div}, \Omega) \mid \gamma_n \boldsymbol{v} = 0 \text{ on } \Gamma_u \text{ and } \gamma_n \boldsymbol{v} \in L^2(\Gamma_o)\},$$

$$\mathcal{B}([p, \boldsymbol{u}], [q, \boldsymbol{v}]) = \mu_p(\partial_t p, q) + (\nabla \cdot \boldsymbol{u}, q) + \mu_u(\partial_t \boldsymbol{u}, \boldsymbol{v}) + (\nabla p, \boldsymbol{v}), \tag{16}$$

$$\mathcal{L}([q, \boldsymbol{v}]) = (f_p, q) + (\boldsymbol{f}_u, \boldsymbol{v}), \tag{17}$$

$$p = 0 \text{ on } \Gamma_p, \qquad \text{strongly imposed}, \tag{18}$$

$$\gamma_n \boldsymbol{u} = 0 \text{ on } \Gamma_u, \quad \text{strongly imposed}, \tag{19}$$

$$\mu_p^{1/2} p = \mu_u^{1/2} \gamma_n \boldsymbol{u} \text{ on } \Gamma_o, \quad \text{strongly imposed}. \tag{20}$$

The variational form II (21)–(25) is obtained integrating by parts the term $(\nabla p, \boldsymbol{v})$, and using the Sommerfeld condition (9) on Γ_o:

$$(\nabla p, \boldsymbol{v}) = -(p, \nabla \cdot \boldsymbol{v}) + \int_{\Gamma_o} \gamma_n \boldsymbol{v} p = -(p, \nabla \cdot \boldsymbol{v}) + \kappa_u \int_{\Gamma_o} \gamma_n \boldsymbol{u} \gamma_n \boldsymbol{v}.$$

The boundary integral on $\Gamma_p \cup \Gamma_u$ vanishes due to (23) and (24) below; the pressure condition on Γ_p is weakly enforced and the velocity condition on Γ_u is strongly enforced. In this case, pressures only need to be in $L^2(\Omega)$, whereas velocities should belong to the same space as in the previous variational form. We observe that the normal trace γ_n of velocity functions have to be in $L^2(\Gamma_o)$ in order to give sense to the Sommerfeld term on Γ_o. In this functional setting, the bilinear/linear forms (21) and (22) are continuous.[2]

Variational form II

$$V_p = L^2(\Omega),$$
$$V_u = \{\boldsymbol{v} \in H(\text{div}, \Omega) \mid \gamma_n \boldsymbol{v} = 0 \text{ on } \Gamma_u \text{ and } \gamma_n \boldsymbol{v} \in L^2(\Gamma_o)\},$$

---

[2] This formulation has already been proposed in [17], but the functional setting was incorrect; only $H(\text{div}, \Omega)$ regularity was assumed for the vector unknowns and the Sommerfeld terms were ill-posed. In any case, the authors explicitly say that this is not the goal of their paper.

$$\mathcal{B}([p,\boldsymbol{u}],[q,\boldsymbol{v}]) = \mu_p(\partial_t p, q) + (\nabla \cdot \boldsymbol{u}, q) + \mu_u(\partial_t \boldsymbol{u}, \boldsymbol{v}) - (p, \nabla \cdot \boldsymbol{v}) + \kappa_u \int_{\Gamma_o} \gamma_n \boldsymbol{v} \gamma_n \boldsymbol{u} \mathrm{d}\Gamma, \tag{21}$$

$$\mathcal{L}([q,\boldsymbol{v}]) = (f_p, q) + (\boldsymbol{f}_u, \boldsymbol{v}), \tag{22}$$

$$p = 0 \text{ on } \Gamma_p, \quad \text{weakly imposed}, \tag{23}$$

$$\gamma_n \boldsymbol{u} = 0 \text{ on } \Gamma_u, \quad \text{strongly imposed}, \tag{24}$$

$$\mu_p^{1/2} p = \mu_u^{1/2} \gamma_n \boldsymbol{u} \text{ on } \Gamma_o, \quad \text{weakly imposed}. \tag{25}$$

Finally, the variational form III (26)–(30) is obtained integrating by parts the term $(\nabla \cdot \boldsymbol{u}, q)$ and proceeding analogously on the boundary:

$$(\nabla \cdot \boldsymbol{u}, q) = -(\boldsymbol{u}, \nabla q) + \int_{\Gamma_o} \gamma_n \boldsymbol{u} q = -(\boldsymbol{u}, \nabla q) + \kappa_p \int_{\Gamma_o} pq.$$

In this case, the velocity condition on Γ_u is weakly enforced, whereas the pressure condition on Γ_p is strongly enforced. The functional setting in this third case is standard.

Variational form III

$$V_p = \{q \in H^1(\Omega) | q = 0 \text{ on } \Gamma_p\}, \quad V_u = L^2(\Omega)^d,$$

$$\mathcal{B}([p,\boldsymbol{u}],[q,\boldsymbol{v}]) = \mu_p(\partial_t p, q) - (\boldsymbol{u}, \nabla q) + \mu_u(\partial_t \boldsymbol{u}, \boldsymbol{v}) + (\nabla p, \boldsymbol{v}) + \kappa_p \int_{\Gamma_o} pq \ \mathrm{d}\Gamma, \tag{26}$$

$$\mathcal{L}([q,\boldsymbol{v}]) = (f_p, q) + (\boldsymbol{f}_u, \boldsymbol{v}), \tag{27}$$

$$p = 0 \text{ on } \Gamma_p, \quad \text{strongly imposed}, \tag{28}$$

$$\gamma_n \boldsymbol{u} = 0 \text{ on } \Gamma_u, \quad \text{weakly imposed}, \tag{29}$$

$$\mu_p^{1/2} p = \mu_u^{1/2} \gamma_n \boldsymbol{u} \text{ on } \Gamma_o, \quad \text{weakly imposed}. \tag{30}$$

Let us note that the Sommerfeld condition on Γ_o is strongly enforced for the first variational form, whereas it is weakly enforced in the other two cases. On the other hand, the introduction of the Sommerfeld boundary conditions requires a more regular functional setting (see [39] for comparison).

Notice the way we have defined V_u for variational forms I and II. When we move from the continuous level to the discrete level we have to ensure the spaces we are working with are complete. The completeness of V_u is proved in the following lemma. A similar result with a similar proof but involving $\boldsymbol{u} \in \boldsymbol{H}$ and $\boldsymbol{u} \times \boldsymbol{n} \in L^2(\Gamma)$ can be found in [40, p. 69, p. 84].

Lemma 2.1 (Completeness of V_u). *The space V_u for the variational forms I and II is complete when it is endowed with the following norm*:

$$|||\boldsymbol{u}|||_{V_u}^2 := \frac{1}{L_0^2} \|\boldsymbol{u}\|^2 + \|\nabla \cdot \boldsymbol{u}\|^2 + \frac{1}{L_0} \|\gamma_n \boldsymbol{u}\|_{L^2(\Gamma_o)}^2. \tag{31}$$

Proof. Let $\{\boldsymbol{u}_n\}$ be a Cauchy sequence in V_u. Since $H(\mathrm{div}, \Omega)$ is complete, $\boldsymbol{u}_n \longrightarrow \boldsymbol{w}$ in $H(\mathrm{div}, \Omega)$. Additionally, $\gamma_n \boldsymbol{u}_n \longrightarrow v$ in $L^2(\Gamma_o)$ since $L^2(\Gamma_o)$ is complete. Furthermore, $\gamma_n \boldsymbol{u}_n \longrightarrow \gamma_n \boldsymbol{w}$ in $H^{-1/2}$ since the normal trace operator γ_n goes from $H(\mathrm{div}, \Omega)$ to $H^{-1/2}$. Since the limits must be the same, we conclude that $\gamma_n \boldsymbol{w} = v$ in $L^2(\Gamma_o)$ and therefore V_u is complete. □

3. Stabilized finite element methods for the wave equation in mixed form

In this section, we present two stabilized FE methods, which we will denote by the acronyms ASGS and OSS, aimed to overcome the instability problems of the standard Galerkin method. In general, the stabilized FE methods we propose can be used with any type of continuous interpolation for p and $\boldsymbol{u}$. In particular, we

focus on equal order continuous interpolations. For conciseness, we consider quasi-uniform FE partitions of size h. For stabilized formulations in general non-uniform non-degenerate cases, see [41].

Let $V_{p,h}$ and $V_{u,h}$ be the FE spaces to approximate p and $\boldsymbol{u}$, respectively, with $V_{p,h} \subset V_p$ and $V_{u,h} \subset V_u$. Additionally, let us define $V_h = V_{p,h} \times V_{u,h}$. For any of these spaces we will make frequent use of the classical inverse inequality $|\nabla v_h| \leqslant C_{\text{inv}} h^{-1} |v_h|$, with C_{inv} a constant independent of the FE function v_h and the mesh size h.

Stabilized FE methods deal with the following problem: Find a pair $[p_h, \boldsymbol{u}_h] \in \mathcal{C}^1(\Upsilon; V_h)$ satisfying the initial conditions $p_h(\boldsymbol{x}, 0) = 0$, $\boldsymbol{u}_h(\boldsymbol{x}, 0) = \boldsymbol{0}$ and such that

$$\mathcal{B}_s([p_h, \boldsymbol{u}_h], [q_h, \boldsymbol{v}_h]) = \mathcal{L}_s([q_h, \boldsymbol{v}_h]) \tag{32}$$

for all test functions $[q_h, \boldsymbol{v}_h] \in V_h$, where the bilinear form $\mathcal{B}_s$ and the linear form $\mathcal{L}_s$ include the Galerkin terms and additional stabilization terms. Depending on how the stabilization part is designed, a different stabilization method arises. Below, we propose two different types of methods, namely ASGS and OSS. The stabilization terms depend on the choice of the so-called stabilization parameters τ_p and τ_u.

3.1. Algebraic sub-grid scale (ASGS) method

The ASGS-type stabilization was originally proposed in [42,43]. The ASGS stabilization terms have the same expression for the three variational forms introduced above. For the wave equation in mixed form, the ASGS stabilized problem (32) is obtained by taking $\mathcal{B}_s$ and $\mathcal{L}_s$ as:

$$\mathcal{B}_s([p_h, \boldsymbol{u}_h], [q_h, \boldsymbol{v}_h]) = \mathcal{B}([p_h, \boldsymbol{u}_h], [q_h, \boldsymbol{v}_h]) + (\mu_p \partial_t p_h + \nabla \cdot \boldsymbol{u}_h, \tau_p \nabla \cdot \boldsymbol{v}_h) + (\mu_u \partial_t \boldsymbol{u}_h + \nabla p_h, \tau_u \nabla q_h), \tag{33}$$

$$\mathcal{L}_s([q_h, \boldsymbol{v}_h]) = \mathcal{L}([q_h, \boldsymbol{v}_h]) + (f_p, \tau_p \nabla \cdot \boldsymbol{v}_h) + (\boldsymbol{f}_u, \tau_u \nabla q_h). \tag{34}$$

It consists in subtracting to the Galerkin terms the integral of the residual of the equation times the adjoint of the spatial differential operator and a stabilization parameter. (τ_u, τ_p) are the stabilization parameters, which will be different for every variational formulation. The additional terms provide stability without harming consistency and a priori error estimates.

3.2. Orthogonal sub-scale stabilization (OSS) method

The OSS stabilization technique was designed in [44,45]. Instead of considering the whole residual (as in ASGS), it only includes quantities that provide stabilization. However, since it would spoil accuracy, the FE projection of these quantities is subtracted, recovering optimal convergence. It consists in solving problem (32) taking $\mathcal{B}_s$ and $\mathcal{L}_s$ as:

$$\mathcal{B}_s([p_h, \boldsymbol{u}_h], [q_h, \boldsymbol{v}_h]) = \mathcal{B}([p_h, \boldsymbol{u}_h], [q_h, \boldsymbol{v}_h]) + \left(P_{p,h}^\perp(\nabla \cdot \boldsymbol{u}_h), \tau_p \nabla \cdot \boldsymbol{v}_h\right) + \left(P_{u,h}^\perp(\nabla p_h), \tau_u \nabla q_h\right), \tag{35}$$

$$\mathcal{L}_s([q_h, \boldsymbol{v}_h]) = \mathcal{L}([q_h, \boldsymbol{v}_h]) + \left(P_{p,h}^\perp(f_p), \tau_p \nabla \cdot \boldsymbol{v}_h\right) + \left(P_{u,h}^\perp(\boldsymbol{f}_u), \tau_u \nabla q_h\right), \tag{36}$$

where $P_{p,h}^\perp(\cdot) = I(\cdot) - P_{p,h}(\cdot)$ and $P_{u,h}^\perp(\cdot) = I(\cdot) - P_{u,h}(\cdot)$, $P_{p,h}(\cdot)$ being the $L^2(\Omega)$ projection on $V_{p,h}$ and $P_{u,h}(\cdot)$ the $L^2(\Omega)$ projection on $V_{u,h}$. This in particular implies that $P_{p,h}(\cdot) = 0$ on Γ_p for variational forms I and III and that $\boldsymbol{n} \cdot P_{u,h}(\cdot) = 0$ on Γ_u for variational forms I and II.

3.3. The stabilization parameters

An important component of stabilized formulations are the stabilization parameters. In our case, we compute them in all formulations as:

$$\tau_p = C_\tau \sqrt{\frac{\mu_u}{\mu_p}} h \sqrt{\frac{\ell_p}{\ell_u}}, \quad \tau_u = C_\tau \sqrt{\frac{\mu_p}{\mu_u}} h \sqrt{\frac{\ell_u}{\ell_p}}, \tag{37}$$

where C_τ is a dimensionless algorithmic constant and ℓ_p, ℓ_u are length scales corresponding to p and $\boldsymbol{u}$ respectively. As it was shown in the analysis presented in [39], in order to mimic at the discrete level the proper functional setting of the continuous problem, the length scales ℓ_p and ℓ_u should be taken as shown in Table 1, where L_0 is a fixed length scale of the problem that can be fixed a priori. The motivation for designing the stabilization parameters can be found in [46,38].

4. Numerical analysis

4.1. Stability analysis

In this section, we present stability results for the ASGS and the OSS methods. We use the concept of Λ-coercivity, originally introduced in [47], which aids us in the proof of stability and convergence analyses. The proofs of the stability lemmata and theorems are very similar to the proofs shown in [39], the only difference being the new terms on Γ_o, due to the Sommerfeld artificial boundary condition. Since these terms have required a more regular functional setting than the one in [39], the working norms now contain the new terms $\kappa_p\|q_h\|^2_{L^2(\Upsilon;L^2(\Gamma_o))}$ and $\kappa_u\|\gamma_n\boldsymbol{v}_h\|^2_{L^2(\Upsilon;L^2(\Gamma_o))}$. These working norms are defined next:

Definition 4.1 (*Working norms*). Let

$$|||[q_h,\boldsymbol{v}_h]|||^2_{0,h} := \mu_p\|q_h\|^2_{L^\infty(\Upsilon;L^2(\Omega))} + \mu_u\|\boldsymbol{v}_h\|^2_{L^\infty(\Upsilon;L^2(\Omega))} + (1+\sigma)\kappa_p\|q_h\|^2_{L^2(\Upsilon;L^2(\Gamma_o))} + (1-\sigma)\kappa_u\|\gamma_n\boldsymbol{v}_h\|^2_{L^2(\Upsilon;L^2(\Gamma_o))}$$

with $\sigma = 0, -1, 1$ for variational forms I, II and III, respectively. We define:

(i) Weak norm:

$$|||[q_h,\boldsymbol{v}_h]|||^2_{W,h} := |||[q_h,\boldsymbol{v}_h]|||^2_{0,h} + \tau_p\|\mu_p\partial_t q_h + \nabla\cdot\boldsymbol{v}_h\|^2_{L^2(\Upsilon;L^2(\Omega))} + \tau_u\|\mu_u\partial_t\boldsymbol{v}_h + \nabla q_h\|^2_{L^2(\Upsilon;L^2(\Omega))}. \tag{38}$$

(ii) Strong norm:

$$|||[q_h,\boldsymbol{v}_h]|||^2_{S,h} := |||[q_h,\boldsymbol{v}_h]|||^2_{0,h} + \tau_p\|\nabla\cdot\boldsymbol{v}_h\|^2_{L^2(\Upsilon;L^2(\Omega))} + \tau_u\|\nabla q_h\|^2_{L^2(\Upsilon;L^2(\Omega))}. \tag{39}$$

We state a first stability result in the form of Λ-coercivity. This concept is used here in the same sense as in [39,47] for the ASGS and OSS methods. The results obtained apply to any of the variational forms, defined in (16), (21), and (26).

In what follows, C denotes a positive constant, independent of μ_p, μ_u, ℓ_p and ℓ_u. In the discrete formulation C will be independent of the mesh size h. The value of C may be different at different occurrences. Additionally, we will use the notation $A \gtrsim B$ and $A \lesssim B$ to indicate that $A \geqslant CB$ and $A \leqslant CB$ respectively, where A and B are two quantities that might depend on the solution or mesh size.

The ASGS and OSS methods are not coercive in the norms of interest and therefore their well-posedness needs to be proved via an inf–sup condition. For the subsequent analysis we use a more descriptive property than the inf–sup condition. This property has been defined as Λ-coercivity in [47].

Definition 4.2 (Λ-*coercivity*). Let $\mathcal{V}$ be a normed space and $\zeta : \mathcal{V} \times \mathcal{V} \longrightarrow \mathbb{R}$ a bilinear form. ζ is Λ-coercive if we can define a continuous operator $\Lambda : \mathcal{V} \longrightarrow \mathcal{V}$, i.e., $\|\Lambda(u)\|_\mathcal{V} \lesssim \|u\|_\mathcal{V} \ \forall u \in \mathcal{V}$, such that

$$\zeta(u, \Lambda(u)) \gtrsim \|u\|_\mathcal{V}\|\Lambda(u)\|_\mathcal{V} \ \forall u \in \mathcal{V}.$$

Table 1
Stabilization parameters order and length scales definition.

Variational form	I	II	III
τ_p	$\mathcal{O}(h)$	$\mathcal{O}(1)$	$\mathcal{O}(h^2)$
τ_u	$\mathcal{O}(h)$	$\mathcal{O}(h^2)$	$\mathcal{O}(1)$
ℓ_p	$\ell_p = \ell_u$	L_0^2/h	h
ℓ_u	$\ell_p = \ell_u$	h	L_0^2/h

Let us recall that the inf–sup condition for ζ implies that $\forall u \in \mathcal{V} \ \exists \ v \in \mathcal{V}$ such that $\zeta(u, v) \gtrsim \|u\|_{\mathcal{V}} \|v\|_{\mathcal{V}}$ with $\|v\|_{\mathcal{V}} \lesssim \|u\|_{\mathcal{V}}$. Thus, Λ-coercivity implies the inf–sup condition for a particular definition of norms but it is stronger, since it also provides a continuous operator Λ that for every function u in $\mathcal{V}$ gives a function $v = \Lambda(u)$ such that the inf–sup condition holds.

In the case of the OSS method we can state Λ-coercivity in two norms: the weak norm defined in (38) and the strong norm defined in (39); ASGS stability can only be proved with the weak norm. The norm in (39) is stronger, since it provides full control over ∇p_h and $\nabla \cdot \boldsymbol{u}_h$. The proof is just a slight modification of the one in [39] to account for the boundary terms and we omit it. We detail the expressions of Λ that allow us to prove Λ-coercivity because they in fact provide information about the stabilization mechanism of every method.

Lemma 4.1 (Λ-coercivity). *Both the ASGS and the OSS methods are Λ-coercive in the norm defined in* (38), *i.e., their associated bilinear form satisfies*

$$|||[q_h, \boldsymbol{v}_h]|||^2_{W,h} \lesssim \int_\Upsilon \mathcal{B}_s([q_h, \boldsymbol{v}_h], \Lambda([q_h, \boldsymbol{v}_h])) \ \mathrm{d}t \quad \forall [q_h, \boldsymbol{v}_h]$$

with the following choices of $\Lambda(\cdot)$:

(i) *ASGS method*:

$$\Lambda([q_h, \boldsymbol{v}_h]) := [q_h + \tau_p \mu_p \partial_t q_h, \boldsymbol{v}_h + \tau_u \mu_u \partial_t \boldsymbol{v}_h],$$

(ii) *OSS method*:

$$\Lambda([q_h, \boldsymbol{v}_h]) := [q_h, \boldsymbol{v}_h] + \beta [\tau_p(\mu_p \partial_t q_h + P_{p,h}(\nabla \cdot \boldsymbol{v}_h)), \tau_u(\mu_u \partial_t \boldsymbol{v}_h + P_{u,h}(\nabla q_h))]$$

with a small enough $\beta > 0$. *Moreover, the OSS method is also Λ-coercive in the norm defined in* (39), *i.e., its bilinear form satisfies*

$$|||[q_h, \boldsymbol{v}_h]|||^2_{S,h} \lesssim \int_\Upsilon \mathcal{B}_s([q_h, \boldsymbol{v}_h], \Lambda_1([q_h, \boldsymbol{v}_h])) \ \mathrm{d}t + \int_\Upsilon \mathcal{B}_s([\partial_t q_h, \partial_t \boldsymbol{v}_h], \Lambda_2([q_h, \boldsymbol{v}_h])) \ \mathrm{d}t$$
$$+ \ \mathcal{B}_s([q_h, \boldsymbol{v}_h], \Lambda_2([q_h, \boldsymbol{v}_h]))|_{t=0}$$

for all $[q_h, \boldsymbol{v}_h]$, *where*

$$\Lambda_1([q_h, \boldsymbol{v}_h]) = [q_h + \beta_1 \tau_p P_{p,h}(\nabla \cdot \boldsymbol{v}_h), \boldsymbol{v}_h + \beta_1 \tau_u P_{u,h}(\nabla q_h)],$$
$$\Lambda_2([q_h, \boldsymbol{v}_h]) = \beta_2 [\partial_t q_h, \partial_t \boldsymbol{v}_h]$$

with $\beta_1 > 0$ *small enough,* $\beta_2 = \mu_p \gamma_p + \mu_u \gamma_u$,

$$\gamma_p = \frac{\alpha}{2} T(\tau_p + \tau_u \frac{\mu_u}{\mu_p}), \quad \gamma_u = \frac{\alpha}{2} T\left(\tau_u + \tau_p \frac{\mu_p}{\mu_u} \right), \tag{40}$$

and $\alpha > 0$ *large enough.*

Now, we state stability of the ASGS and the OSS methods. The results obtained apply to any of the variational forms defined in (16)–(30). We start defining the norms in which the external forces need to be bounded in order to obtain stability. Again, it provides information about the behavior of the two formulations considered and, obviously, the regularity requirements on the data in order to have well-posedness.

Definition 4.3 (*External Forces Norms*). Let us consider the following norms of the data:

(i) External forces weak norm for the OSS method:

$$\|[f_p, \boldsymbol{f}_u]\|^2_{\text{W-OSS},h} := \frac{1}{\mu_p} \|f_p\|^2_{L^1(\Upsilon, L^2(\Omega))} + \frac{1}{\mu_u} \|\boldsymbol{f}_u\|^2_{L^1(\Upsilon, L^2(\Omega))} + \tau_p \|f_p\|^2_{L^2(\Upsilon, L^2(\Omega))} + \tau_u \|\boldsymbol{f}_u\|^2_{L^2(\Upsilon, L^2(\Omega))}. \tag{41}$$

(ii) External forces weak norm for the ASGS method:

$$\|[f_p, \boldsymbol{f}_u]\|^2_{\text{W-ASGS},h} := \|[f_p, \boldsymbol{f}_u]\|^2_{\text{W-OSS},h} + \tau_p \tau_u \mu_u \|\partial_t f_p\|^2_{L^1(\Upsilon, L^2(\Omega))} + \tau_p \tau_u \mu_p \|\partial_t \boldsymbol{f}_u\|^2_{L^1(\Upsilon, L^2(\Omega))}$$
$$+ \tau_p \tau_u \mu_u \|f_p\|^2_{L^\infty(\Upsilon, L^2(\Omega))} + \tau_p \tau_u \mu_p \|\boldsymbol{f}_u\|^2_{L^\infty(\Upsilon, L^2(\Omega))}. \tag{42}$$

(iii) External forces strong norm for the OSS method:

$$\|[f_p, \boldsymbol{f}_u]\|^2_{\text{S-OSS},h} := \|[f_p, \boldsymbol{f}_u]\|^2_{\text{W-OSS},h} + \gamma_p \Big(\|\partial_t f_p\|^2_{L^1(\Upsilon, L^2(\Omega))} + \|f_p(0)\|^2 \Big) + \gamma_u \Big(\|\partial_t \boldsymbol{f}_u\|^2_{L^1(\Upsilon, L^2(\Omega))} + \|\boldsymbol{f}_u(0)\|^2 \Big)$$
$$+ \beta_2 \tau_p \|\partial_t f_p\|^2_{L^2(\Upsilon, L^2(\Omega))} + \beta_2 \tau_u \|\partial_t \boldsymbol{f}_u\|^2_{L^2(\Upsilon, L^2(\Omega))} \tag{43}$$

with γ_p and γ_u given in (40).

Next, we state the stability properties of the different methods. Their proof is very similar to the ones in [39], the only modification being the boundary terms arising from the Sommerfeld boundary condition.

Theorem 4.1 (*Stability*). *The solution* $[p_h, \boldsymbol{u}_h]$ *of the ASGS-stabilized FE formulation* (32) *with* (33) *and* (34) *satisfies*

$$\||[p_h, \boldsymbol{u}_h]\||^2_{W,h} \lesssim \|[f_p, \boldsymbol{f}_u]\|^2_{\text{W-ASGS},h} \tag{44}$$

with the norms defined in (38) *and* (42). *On the other hand, the solution of the OSS-stabilized FE formulation* (32) *with* (35) *and* (36) *satisfies*

$$\||[p_h, \boldsymbol{u}_h]\||^2_{W,h} \lesssim \|[f_p, \boldsymbol{f}_u]\|^2_{\text{W-OSS},h} \tag{45}$$

with the (weak) norms defined in (38) *and* (41), *as well as*

$$\||[p_h, \boldsymbol{u}_h]\||^2_{S,h} \lesssim \|[f_p, \boldsymbol{f}_u]\|^2_{\text{S-OSS},h} \tag{46}$$

with the (strong) norms defined in (39) *and* (43).

4.2. Convergence analysis

In this section we present convergence results for the stabilized FE methods proposed. The results obtained apply to any of the variational forms defined in (16)–(30). Once again, the proof is omitted because it is very similar to the proofs presented in [39], the only difference being the treatment of the boundary terms arising from the Sommerfeld condition. The way to deal with them is shown in the following lemma.

Let us define p_I as the $P_{p,h}$ projection of the exact solution p on $V_{p,h}$ and $\boldsymbol{u}_I$ as the $P_{u,h}$ projection of the exact solution $\boldsymbol{u}$ on $V_{u,h}$. This projection, which, contrary to the classical L^2 projection, incorporates boundary conditions, turns out to be optimal:

Lemma 4.2 (*Optimality of* $P_{p,h}$ *and* $P_{u,h}$). *Let* $P_{p,h} : V_p \longrightarrow V_{p,h}$ *and* $P_{u,h} : V_u \longrightarrow V_{u,h}$ *be two projections defined as*:

$$(P_{p,h}(q), \chi_h) = (q, \chi_h) \quad \forall \chi_h \in V_{p,h}, \quad P_{p,h}(q) = 0 \text{ on } \Gamma_p,$$
$$(P_{u,h}(\boldsymbol{v}), \boldsymbol{w}_h) = (\boldsymbol{v}, \boldsymbol{w}_h) \quad \forall \boldsymbol{w}_h \in V_{u,h}, \quad \boldsymbol{n} \cdot P_{u,h}(\boldsymbol{v}) = 0 \text{ on } \Gamma_u.$$

Let k and l be the polynomial interpolation order for $V_{p,h}$ *and* $V_{u,h}$, *respectively. Then,* $P_{p,h}$ *and* $P_{u,h}$ *are optimal in* $L^2(\Omega)$, $H^1(\Omega)$ *and* $L^2(\Gamma)$, *that is to say*:

$$\|q - P_{p,h}(q)\|_{L^2(\Omega)} \lesssim h^{k+1} |q|_{H}^{k+1}(\Omega), \quad \|\boldsymbol{v} - P_{u,h}(\boldsymbol{v})\|_{L^2(\Omega)} \lesssim h^{l+1} |\boldsymbol{v}|_{H}^{l+1}(\Omega),$$
$$\|q - P_{p,h}(q)\|_{H}^1(\Omega) \lesssim h^k |q|_{H}^{k+1}(\Omega), \quad \|\boldsymbol{v} - P_{u,h}(\boldsymbol{v})\|_{H}^1(\Omega) \lesssim h^l |\boldsymbol{v}|_{H}^{l+1}(\Omega),$$
$$\|q - P_{p,h}(q)\|_{L}^2(\Gamma) \lesssim h^{k+\frac{1}{2}} |q|_{H^{k+\frac{1}{2}}(\Gamma)}, \quad \|\gamma_n \boldsymbol{v} - \gamma_n P_{u,h}(\boldsymbol{v})\|_{L}^2(\Gamma) \lesssim h^{l+\frac{1}{2}} |\boldsymbol{v}|_{H}^{l+\frac{1}{2}}(\Gamma),$$

for smooth enough $q \in V_p$ *and* $\boldsymbol{v} \in V_u$.

Proof. The proof follows the one in [39]. The additional ingredient is the error estimate for the boundary terms, whose proof is a straightforward consequence of the classical interpolation estimates for traces of functions on boundaries. Note that $P_{p,h}(q) = q$ on Γ_p and $\gamma_n P_{u,h}(\boldsymbol{v}) = \gamma_n \boldsymbol{v}$ on Γ_u. $\quad\square$

Let us define two types of error functions. The error of the approximate solution (obtained using the ASGS or the OSS methods) with respect to the projected exact solution is defined as:

$$e_p := p_h - p_I, \quad \boldsymbol{e}_u := \boldsymbol{u}_h - \boldsymbol{u}_I,$$

whereas the error of the exact solution with respect to the projected exact solution is defined as:

$$\varepsilon_p := p - p_I, \quad \boldsymbol{\varepsilon}_u := \boldsymbol{u} - \boldsymbol{u}_I.$$

Notice that $[e_p, \boldsymbol{e}_u]$ belongs to the FE space and $[\varepsilon_p, \boldsymbol{\varepsilon}_u]$ is orthogonal to the FE space with respect to the $L^2(\Omega)$ inner product.

Definition 4.4 (*Error Functions*). Let us define the following error functions:

(i) OSS weak error function:

$$
\begin{aligned}
E^2_{\text{W-OSS}}(h) := {} & \mu_p\|\varepsilon_p\|^2_{L^\infty(\Upsilon,L^2(\Omega))} + \mu_u\|\boldsymbol{\varepsilon}_u\|^2_{L^\infty(\Upsilon,L^2(\Omega))} + \tau_u\|\nabla\varepsilon_p\|^2_{L^2(\Upsilon,L^2(\Omega))} + \tau_p\|\nabla\cdot\boldsymbol{\varepsilon}_u\|^2_{L^2(\Upsilon,L^2(\Omega))} \\
& + \tau_p\|\mu_p\partial_t\varepsilon_p\|^2_{L^2(\Upsilon,L^2(\Omega))} + \tau_u\|\mu_u\partial_t\boldsymbol{\varepsilon}_u\|^2_{L^2(\Upsilon,L^2(\Omega))} + \frac{1}{\tau_p}\|\varepsilon_p\|^2_{L^2(\Upsilon,L^2(\Omega))} + \frac{1}{\tau_u}\|\boldsymbol{\varepsilon}_u\|^2_{L^2(\Upsilon,L^2(\Omega))} \\
& + (1+\sigma)\kappa_p\|\varepsilon_p\|^2_{L^2(\Upsilon,L^2(\Gamma_o))} + (1-\sigma)\kappa_u\|\gamma_n\boldsymbol{\varepsilon}_u\|^2_{L^2(\Upsilon,L^2(\Gamma_o))}.
\end{aligned}
\tag{47}
$$

(ii) ASGS error function:

$$
\begin{aligned}
E^2_{\text{W-ASGS}}(h) := {} & E^2_{\text{W-OSS}}(h) + \mu_u\tau_p\tau_u\|\mu_p\partial_t\varepsilon_p\|^2_{L^\infty(\Upsilon,L^2(\Omega))} + \mu_p\tau_p\tau_u\|\mu_u\partial_t\boldsymbol{\varepsilon}_u\|^2_{L^\infty(\Upsilon,L^2(\Omega))} + \mu_u\tau_p\tau_u\|\mu_p\partial_{tt}\varepsilon_p\|^2_{L^1(\Upsilon,L^2(\Omega))} \\
& + \mu_p\tau_p\tau_u\|\mu_u\partial_{tt}\boldsymbol{\varepsilon}_u\|^2_{L^1(\Upsilon,L^2(\Omega))} + \mu_p\tau_p\tau_u\|\nabla\varepsilon_p\|^2_{L^\infty(\Upsilon,L^2(\Omega))} + \mu_u\tau_p\tau_u\|\nabla\cdot\boldsymbol{\varepsilon}_u\|^2_{L^\infty(\Upsilon,L^2(\Omega))} \\
& + \mu_p\tau_p\tau_u\|\nabla\partial_t\varepsilon_p\|^2_{L^1(\Upsilon,L^2(\Omega))} + \mu_u\tau_p\tau_u\|\nabla\cdot\partial_t\boldsymbol{\varepsilon}_u\|^2_{L^1(\Upsilon,L^2(\Omega))}.
\end{aligned}
\tag{48}
$$

(iii) OSS strong error function:

$$
\begin{aligned}
E^2_{\text{S-OSS}}(h) := {} & E^2_{\text{W-OSS}}(h) + \gamma_p\|\mu_p\partial_{tt}\varepsilon_p + \nabla\cdot\partial_t\boldsymbol{\varepsilon}_u\|^2_{L^1(\Upsilon,L^2(\Omega))} + \gamma_u\|\mu_u\partial_{tt}\boldsymbol{\varepsilon}_u + \nabla\partial_t\varepsilon_p\|^2_{L^1(\Upsilon,L^2(\Omega))}\beta_2\tau_p\|\nabla\cdot\partial_t\boldsymbol{\varepsilon}_u\|^2_{L^2(\Upsilon,L^2(\Omega))} \\
& + \beta_2\tau_u\|\nabla\partial_t\varepsilon_p\|^2_{L^2(\Upsilon,L^2(\Omega))} + \gamma_p\|\mu_p\partial_t\varepsilon_p(0)\|^2 + \gamma_u\|\mu_u\partial_t\boldsymbol{\varepsilon}_u(0)\|^2.
\end{aligned}
\tag{49}
$$

The following theorem shows that the previous error functions are in fact the upper bounds for the error of the methods we consider. The proof follows the same lines as in [39].

Theorem 4.2 (*Convergence*). *Let $[p, \boldsymbol{u}]$ be the solution of the continuous problem* (15) *and let $[p_h, \boldsymbol{u}_h]$ be the solution of the stabilized discrete problem* (32). *For the ASGS formulation* (33) *and* (34), *the discrete solution satisfies the following error estimate*:

$$|||[p - p_h, \boldsymbol{u} - \boldsymbol{u}_h]|||_{W,h} \lesssim E_{\text{W-ASGS}}(h) \tag{50}$$

with the norm defined in (38) *and the error function* (48). *On the other hand, the OSS formulation* (35) *and* (36) *satisfies*

$$|||[p - p_h, \boldsymbol{u} - \boldsymbol{u}_h]|||_{W,h} \lesssim E_{\text{W-OSS}}(h) \tag{51}$$

with the norm defined in (38) *and the error function* (47), *as well as*

$$|||[p - p_h, \boldsymbol{u} - \boldsymbol{u}_h]|||_{S,h} \lesssim E_{\text{S-OSS}}(h) \tag{52}$$

with the norm (39) *and the error function* (49).

4.3. Accuracy of ASGS and OSS Methods

Let k be the order of p-interpolation and l the order of $\boldsymbol{u}$-interpolation. Analyzing the a priori error estimates for the ASGS and the OSS methods from (50) and (51) and assuming regular enough solutions, we can summarize the convergence rates of the formulations as shown in Table 2. Further, the OSS method also satisfies the error estimate in the strong norm (52), summarized in Table 3. We stress the fact that the convergence rates do depend on the choice of the stabilization parameters, and different convergence orders are obtained for the three discrete variational formulations above. We note that the introduction of Sommerfeld artificial boundary conditions does not spoil the convergence rates in [39].

5. Numerical experiments

In this section we perform numerical experiments with the finite element formulations presented. First, in Section 5.1, we test convergence in h. To achieve that, we choose an analytical solution that *satisfies* the boundary conditions. This experiment shows the convergence of the discrete solution to the analytical solution. The intention of this experiment is just to check the convergence in h of the stabilization methods for all variational forms. Additionally, the intention is not to evaluate the accuracy of the NRBC because that is done later on in Section 5.2.

Then, in Section 5.2, we evaluate the accuracy of the NRBC. The main objective is to evaluate how good is the NRBC compared to the solution obtained in an unbounded domain. As the NRBC is not exact, we show that the error of the discrete solution using the NRBC with respect to the solution in the unbounded domain does not approach zero as we refine the mesh. This is the error introduced by the NRBC. Additionally, in Section 5.2.5, we evaluate the error as a function of the NRBC location.

5.1. Convergence tests

Let us consider a two-dimensional transient problem with analytical solution to investigate the convergence properties of the stabilized FE formulations proposed. We take $\Omega = (0, 1) \times (0, 1)$, the time interval $[0, 0.01]$, physical properties $\mu_p = 10.0$ and $\mu_u = 10.0$, and the forcing terms f_p and $\boldsymbol{f}_u$ such that the exact solution is:

Table 2
Convergence rates according to the variational forms for the ASGS and OSS methods in the weak norm.

Variational form	I	II	III
$\|p - p_h\|_{L^\infty(\Upsilon, L^2(\Omega))}$	$h^{k+1/2} + h^{l+1/2}$ Quasi-optimal	$h^{k+1/2} + h^l$ Suboptimal	$h^k + h^{l+1/2}$ Suboptimal
$\|\boldsymbol{u} - \boldsymbol{u}_h\|_{L^\infty(\Upsilon, L^2(\Omega))}$	$h^{k+1/2} + h^{l+1/2}$ Quasi-optimal	$h^{k+1/2} + h^l$ Suboptimal	$h^k + h^{l+1/2}$ Suboptimal
$\|\mu_u \partial_t(\boldsymbol{u} - \boldsymbol{u}_h) + \nabla(p - p_h)\|_{L^2(\Upsilon, L^2(\Omega))}$	$h^k + h^l$ Optimal	$h^{k-1/2} + h^{l-1}$ Suboptimal	$h^k + h^{l+1/2}$ Optimal
$\|\mu_p \partial_t(p - p_h) + \nabla \cdot (\boldsymbol{u} - \boldsymbol{u}_h)\|_{L^2(\Upsilon, L^2(\Omega))}$	$h^k + h^l$ Optimal	$h^{k+1/2} + h^l$ Optimal	$h^{k-1} + h^{l-1/2}$ Suboptimal
k, l Optimal	$k = l$	$k + 1/2 = l$	$k = l + 1/2$

Table 3
Convergence rates according to the variational forms for the OSS method in the strong norm.

Variational form	I	II	III
$\|\nabla(p - p_h)\|_{L^2(\Upsilon, L^2(\Omega))}$	$h^k + h^l$ Optimal	$h^{k-1} + h^{l-1}$ Suboptimal	$h^k + h^l$ Optimal
$\|\nabla \cdot (\boldsymbol{u} - \boldsymbol{u}_h)\|_{L^2(\Upsilon, L^2(\Omega))}$	$h^k + h^l$ Optimal	$h^k + h^l$ Optimal	$h^{k-1} + h^{l-1}$ Suboptimal
k, l Optimal	$k = l$	$k = l$	$k = l$

$$p = \sin\left(\frac{3}{2}\pi x\right)\sin(3\pi y)\sin(2\pi t), \quad \boldsymbol{u} = [p, p].$$

We impose $p = 0$ on $x = 0$, $y = 0$ and $y = 1$. The NRBC is imposed on $x = 1$.

For the spatial discretization, we have used four uniform FE meshes with $h = 0.010$, $h = 0.005$, $h = 0.002$ and $h = 0.001$. The elements used are $P1$ (three-node triangular elements) and $P2$ (six-node triangular elements). Fig. 1 shows the mesh for $h = 0.10$. The other meshes are isotropic refinements of that one.

The stabilization parameters are computed with the algorithmic constant $C_\tau = 0.01$ for $P1$ elements and with $C_\tau = 0.4$ for $P2$ elements. The characteristic domain length was taken as $L_0 = \sqrt[d]{\text{meas}(\Omega)} = 1$. The time integration scheme is Crank–Nicolson with a time step size of 10^{-5}. We have used a very small time step to avoid any interference of the time marching algorithm into the spatial error since we are only interested in the spatial error. With that time step size, the difference between the error of the scalar unknown in the norm $\|\cdot\|_{L^\infty(\Upsilon, L^2(\Omega))}$ and the error in the same norm with a time step size twice as big was less than 1% in the finest mesh.

In Tables 4–7 the experimental convergence rates for the ASGS and the OSS methods are shown. In the tables, the word Num stands for the numerical result and the word Min stands for the minimum expected convergence rate based on theoretical analysis. All these numerical results match or are better than the convergence rates predicted theoretically.

5.2. NRB performance evaluation

Many benchmark problems have been devised in order to evaluate the performance of NRBC and NRBL formulations. Some procedures compare an analytical solution with the numerical solution in the truncated
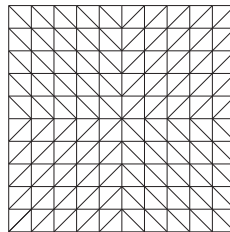
Fig. 1. Mesh sample.

Table 4
Experimental convergence rates for the ASGS method using $P1/P1$ interpolation.

Variational form	I		II		III	
Boundary cond.	Num	Min	Num	Min	Num	Min
$\|p - p_h\|_{L^\infty(\Upsilon, L^2(\Omega))}$	2.01	1.5	1.97	1	1.98	1
$\|\boldsymbol{u} - \boldsymbol{u}_h\|_{L^\infty(\Upsilon, L^2(\Omega))}$	2.01	1.5	1.99	1	2.01	1
$\|\nabla(p - p_h)\|_{L^2(\Upsilon, L^2(\Omega))}$	1.00	1	1.00	0	1.00	1
$\|\nabla \cdot (\boldsymbol{u} - \boldsymbol{u}_h)\|_{L^2(\Upsilon, L^2(\Omega))}$	1.00	1	1.00	1	1.00	0

Table 5
Experimental convergence rates for the OSS method using $P1/P1$ interpolation.

Variational form	I		II		III	
Boundary Cond.	Num	Min	Num	Min	Num	Min
$\|p - p_h\|_{L^\infty(\Upsilon, L^2(\Omega))}$	2.01	1.5	1.97	1	1.98	1
$\|\boldsymbol{u} - \boldsymbol{u}_h\|_{L^\infty(\Upsilon, L^2(\Omega))}$	2.01	1.5	1.99	1	2.01	1
$\|\nabla(p - p_h)\|_{L^2(\Upsilon, L^2(\Omega))}$	1.00	1	1.00	0	1.00	1
$\|\nabla \cdot (\boldsymbol{u} - \boldsymbol{u}_h)\|_{L^2(\Upsilon, L^2(\Omega))}$	1.00	1	1.00	1	1.00	0

Table 6
Experimental convergence rates for the ASGS method using $P2/P2$ interpolation.

Variational form	I		II		III	
Boundary cond.	Num	Min	Num	Min	Num	Min
$\|p - p_h\|_{L^\infty(\Upsilon, L^2(\Omega))}$	3.04	2.5	2.67	2	3.41	2
$\|\boldsymbol{u} - \boldsymbol{u}_h\|_{L^\infty(\Upsilon, L^2(\Omega))}$	3.01	2.5	2.62	2	2.77	2
$\|\nabla(p - p_h)\|_{L^2(\Upsilon, L^2(\Omega))}$	2.07	2	1.78	1	2.56	2
$\|\nabla \cdot (\boldsymbol{u} - \boldsymbol{u}_h)\|_{L^2(\Upsilon, L^2(\Omega))}$	2.08	2	2.57	2	1.78	1

Table 7
Experimental convergence rates for the OSS method using $P2/P2$ interpolation.

Variational form	I		II		III	
Boundary cond.	Num	Min	Num	Min	Num	Min
$\|p - p_h\|_{L^\infty(\Upsilon, L^2(\Omega))}$	3.00	2.5	2.64	2	3.17	2
$\|\boldsymbol{u} - \boldsymbol{u}_h\|_{L^\infty(\Upsilon, L^2(\Omega))}$	3.00	2.5	2.48	2	2.75	2
$\|\nabla(p - p_h)\|_{L^2(\Upsilon, L^2(\Omega))}$	2.06	2	1.78	1	2.54	2
$\|\nabla \cdot (\boldsymbol{u} - \boldsymbol{u}_h)\|_{L^2(\Upsilon, L^2(\Omega))}$	2.06	2	2.53	2	1.78	1

domain using the NRB, e.g., Problems 1 and 2 in Category 3 of [48]. Other examples are the Parts 1, 2 and 3 of Problem 3 in Category 1 of [49]. Other procedures involve solving the problem in a truncated domain and in a bigger domain, and compare the solution of the big domain restricted to the truncated domain with the solution obtained in the truncated domain with the NRB [6,18].

5.2.1. Benchmark problem with analytical solution

Let us consider Problem 1-Category 3 proposed in [48]. This problem has also appeared in [9]. The 2D ($d = 2$) spatial domain is taken as $\Omega = (-100, 100) \times (-100, 100)$ The physical parameters are taken as $\mu_u = 1$, $\mu_p = 1$. In all the boundary Γ of the domain NRBCs are imposed. In the references mentioned, the problem is solved with a Mach number $(M, 0)$ (mean flow in the x direction). In this work we have considered the non-convected wave equation and therefore we take $M = 0$ (zero mean flow). The simulation time is $T = 150$. The time step is taken as 1.0 and the time integration scheme used is BDF2. The initial condition is:

$$p = \exp\left[-(\ln 2)\left(\frac{x^2 + y^2}{\delta_a^2}\right)\right], \quad u_1 = 0, \quad u_2 = 0,$$

where $\delta_a = 20$ is the radius of the acoustic pulse. The problem consists in finding the unknowns at various instants of time.

Let $\alpha_1 = \frac{\ln 2}{\delta_a^2}$ and $\eta = \sqrt{x^2 + y^2}$. The exact solution is:

$$p = \frac{1}{2\alpha_1} \int_0^\infty e^{\frac{-\xi^2}{4\alpha_1}} \cos(\xi t) J_0(\xi\eta)\xi \, d\xi,$$

$$u_1 = \frac{x}{2\alpha_1\eta} \int_0^\infty e^{\frac{-\xi^2}{4\alpha_1}} \sin(\xi t) J_1(\xi\eta)\xi \, d\xi,$$

$$u_2 = \frac{y}{2\alpha_1\eta} \int_0^\infty e^{\frac{-\xi^2}{4\alpha_1}} \sin(\xi t) J_1(\xi\eta)\xi \, d\xi,$$

where J_α are the Bessel functions of first kind of order α.

The mesh used to solve the problem was a structured mesh of various element sizes, ranging from $h = 20$ (10 elements per direction) to $h = 2$ (100 elements per direction). Fig. 2 shows the contours of the discrete solution p_h at $t = 0$, $t = 50$ and $t = 150$, computed using variational form I (VF I) and the ASGS method on the mesh with $h = 5$. Fig. 3 shows the contours of the exact solution p at $t = 0$, 50 and 150. These figures are only
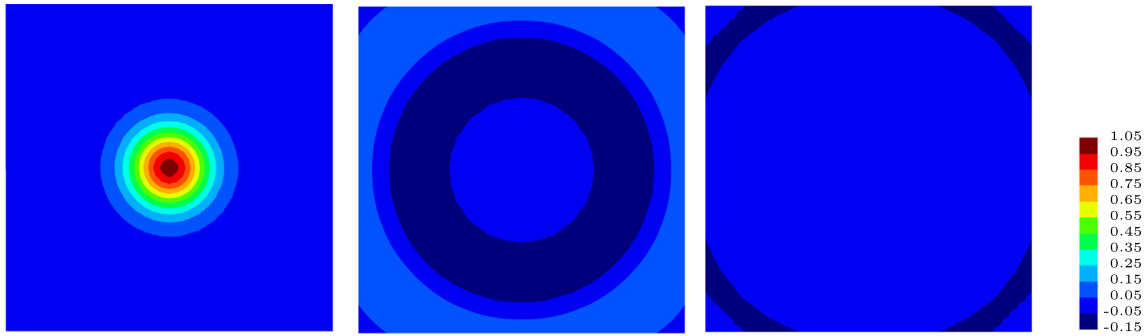
Fig. 2. Contours of p_h for the benchmark problem with analytical solution (ASGS method, VF I, $h = 5$).
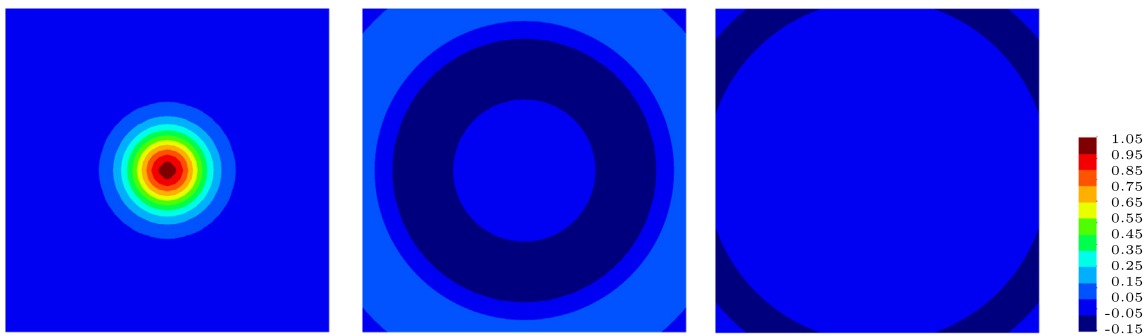

Fig. 3. Contours of the exact p for the benchmark problem with analytical solution.

intended to illustrate the type of solution of this problem and how the numerical solution behaves. Approximate solutions obtained with other variational forms or with the OSS method are qualitatively very similar.

Fig. 4 shows a cut along $y = 0$ from $x = 0$ to $x = 100$ of p_h, and compares it with the analytical solution at $t = 50$, 100 and 150. Fig. 5 shows a cut along $x = y$ from $(x, y) = 0$ to $(x, y) = (100, 100)$ of p_h and compares it with the analytical solution at the same time instants. Once again, the discrete solution corresponds to the ASGS method, VF I and $h = 5$.

In Table 8 the results obtained are shown for various mesh sizes, polynomial interpolations, stabilization methods and variational forms. The error is computed as the $L^\infty(\Upsilon, L^2(\Omega))$-norm of the numerical solution respect to the exact solution and it is normalized by the $L^\infty(\Upsilon, L^2(\Omega))$-norm of the exact solution. For VF II and III, the characteristic length is taken as $L_0 = 100$. The algorithmic constant is taken as $C_\tau = 0.05$ for linear elements and $C_\tau = 0.1$ for quadratic elements in 2D and $C_\tau = 0.1$ for linear elements in 3D. We have
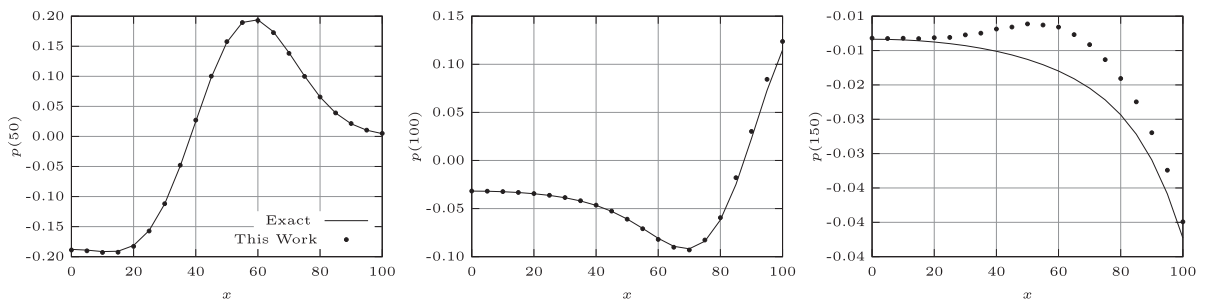
Fig. 4. Cut at $y = 0$ of p for the benchmark problem with analytical solution (ASGS method, VF I, $h = 5$, Q1 elements, $C_\tau = 0.05$). Results shown at $t = 50$, 100 and 150.
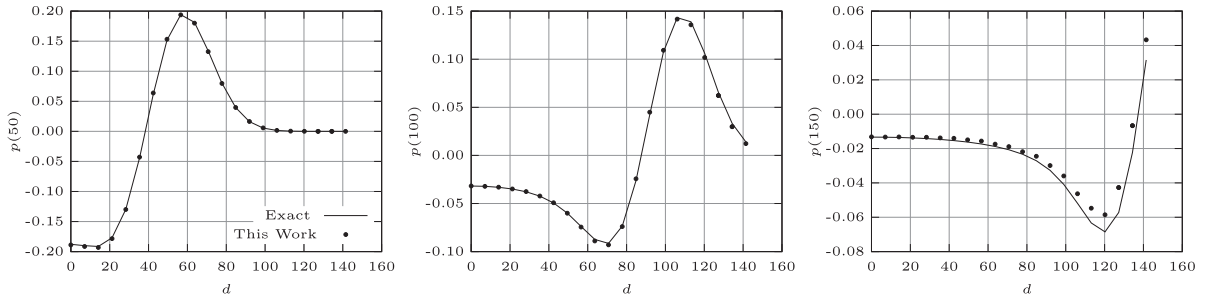
Fig. 5. Cut at $x = y$ of p for the benchmark problem with analytical solution (ASGS method, VF I, $h = 5$, Q1 elements, $C_\tau = 0.05$). Results shown at $t = 50$, 100 and 150.

Table 8
Error of the NRBC for the benchmark problem with analytical solution.

h	Element	Method	VF	Error in p	Error in $\boldsymbol{u}$
20	Q1	ASGS	I	0.2166	0.2571
20	Q2	ASGS	I	0.1120	0.1398
5	Q1	ASGS	I	0.0385	0.0894
5	Q2	ASGS	I	0.0379	0.0903
2	Q1	ASGS	I	0.0383	0.0912
2	Q2	ASGS	I	0.0384	0.0916
5	Q1	ASGS	II	0.0439	0.0934
5	Q1	ASGS	III	0.0443	0.0935
5	Q1	OSS	I	0.0386	0.0897

found experimentally that these values yield good results, and are the values used in all the examples. Note that in all cases the error behaves as expected. When the error does not decrease as the mesh is refined or the polynomial order is increased, it is because of the error introduced by the NRBC.

5.2.2. Big/small domain benchmark problem in 2D

A very interesting NRB performance test appeared in [18]. Using SI units throughout, the problem proposed is defined on a square domain of side 10 000 centered at the origin of coordinates and divided into 100×100 Q1 elements, with the NRB condition on the four sides. The reference state properties are density $\rho_0 = 1.2$, pressure $p_0 = 1.01 \times 10^5$ and heat capacity ratio $\gamma = 1.4$. We take $\mu_p = \frac{1}{\gamma p_0}$, $\mu_u = \rho_0$ and the initial condition is

$$p(\boldsymbol{x}, 0) = \begin{cases} 0.01\, p_0 \cos\left(\frac{\pi r}{2R}\right) & \text{if } r < R, \\ 0 & \text{otherwise} \end{cases}$$

with $R = 1000$ and $r = \sqrt{x^2 + y^2}$. The simulation time is $T = 24$.

For comparison, a reference solution is obtained in a bigger domain, namely, a square of side 30 000 with the region of interest in its center. The boundary condition used in the big domain is $p = 0$ everywhere. The big domain is discretized with a mesh of 300×300 Q1 elements.

Let us denote as $[p_h, \boldsymbol{u}_h]$ the solution in the small domain and as $[p_{R,h}, \boldsymbol{u}_{R,h}]$ the solution in the big domain. The error is computed as:

$$e_p = \left(\max_t \sqrt{\sum_{n=1}^{N} (p_{R,h}(\boldsymbol{x}_n, t) - p_h(\boldsymbol{x}_n, t))^2} \right) \left(\max_t \sqrt{\sum_{n=1}^{N} (p_{R,h}(\boldsymbol{x}_n, t))^2} \right)^{-1}, \tag{53}$$

where N is the number of nodes of the problem in the small domain, with coordinates $\boldsymbol{x}_n$, $n = 1, \ldots, N$. The error for the x-component and y-component of $\boldsymbol{u}$ (e_u and e_v, respectively) is computed similarly.

To get an qualitative impression of the type of solution we are looking for and how the NRBC behaves, Fig. 6 shows the contours of p_h in the small domain at $t = 0$, 8 and 16, whereas Fig. 7 shows the contours of $p_{R,h}$ in the same region and at the same time instants. As in the previous example, these solutions have been computed using VF I and the ASGS method.

Fig. 8 shows a cut at $y = 0$ for $0 \leqslant x \leqslant 5000$ of p_h and compares it with the solution $p_{R,h}$ obtained in the big domain at $t = 8$, 16 and 24. Fig. 9 shows a similar cut and at the same time instants, but along $x = y$ from $(x, y) = (0, 0)$ to $(x, y) = (5000, 5000)$. It is observed that the solutions in the big and small domains only differ significantly at $t = 24$, where a certain reflection is observed in spite of using the Sommerfeld boundary condition. However, these reflections are very small. To see this, Fig. 10 shows the evolution in time of the energy
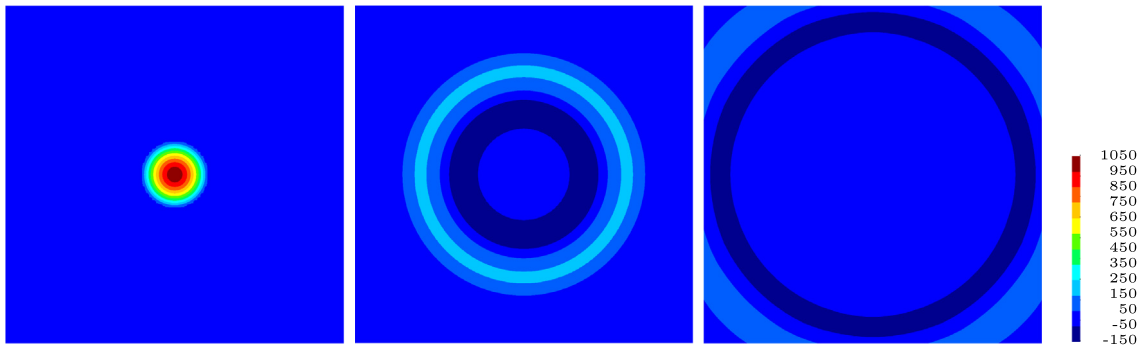
Fig. 6. Contours of p_h in the small domain for the big/small domain benchmark problem in 2D. From the left to the right: $t = 8$, $t = 16$ and $t = 24$.
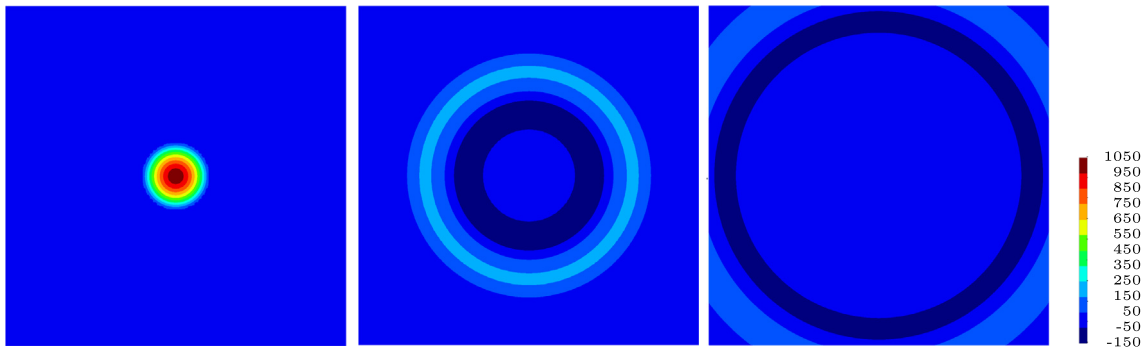
Fig. 7. Contours of $p_{R,h}$ in the big domain for the big/small domain benchmark problem in 2D. From the left to the right: $t = 8$, $t = 16$ and $t = 24$.
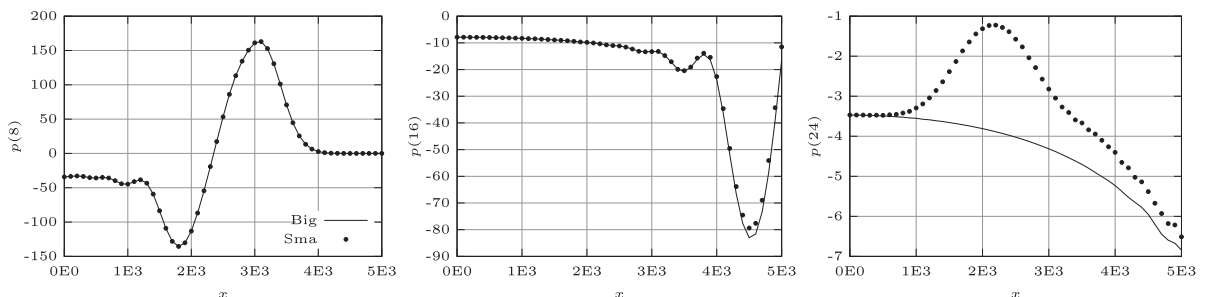
Fig. 8. Cut at $y = 0$ of p_h and $p_{R,h}$ for the big/small domain benchmark problem in 2D. From the left to the right: $t = 8$, $t = 16$ and $t = 24$.
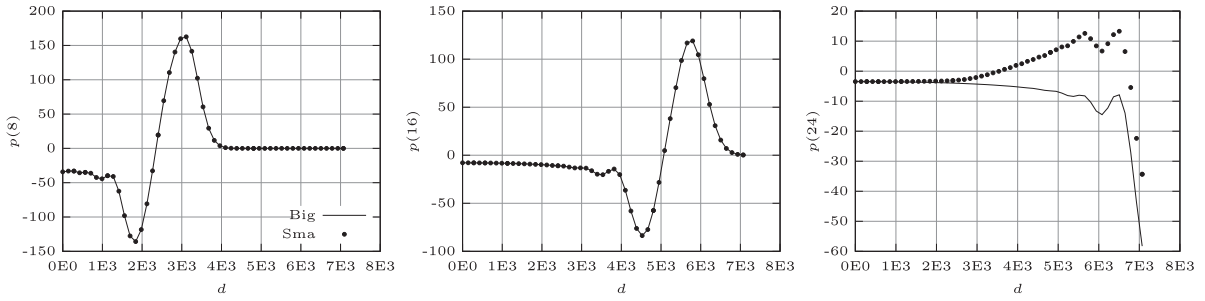
Fig. 9. Cut at $x = y$ of p_h and $p_{R,h}$ for the big/small domain benchmark problem in 2D. From the left to the right: $t = 8$, $t = 16$ and $t = 24$.
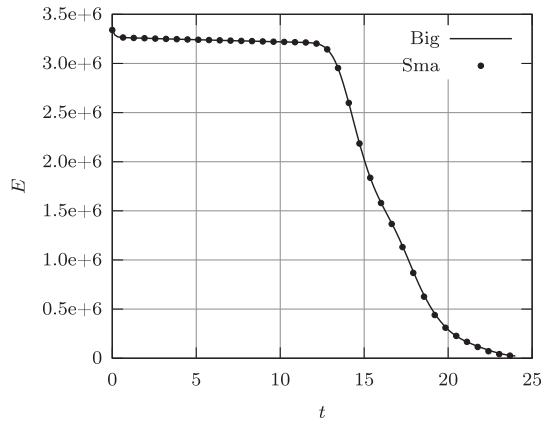
Fig. 10. Evolution of total energy E for the big/small domain benchmark problem in 2D.

E in the region of interest. It can be seen that the solution in the small domain with the NRBC behaves as the big domain solution.

The results obtained with the NRBC are presented in Table 9 for various mesh sizes (100 and 50), polynomial order (P1 and P2), stabilization methods (ASGS and OSS), variational forms (I, II and III), domain length scales (10, 100 and 1000), time marching schemes (Crank Nicolson and 2nd order BDF) and time step sizes ($\delta t = 0.16$ and 0.08). It can be seen that the error for p is around 5.8% and the error for u is around 8.2% for all cases, independently of the numerical strategy. It can therefore be concluded that this error comes exclusively from the truncation of the domain with the NRBC. In [18] the errors reported are $e_p = 2.9\%$ and $e_u = e_v = 6.2\%$ for a NRBC of order $J = 10$, slightly smaller than those we have found. Additionally, the errors obtained with our formulation are similar to the ones obtained with $J = 7$. A second order finite

Table 9
Error of the NRBC for the big/small domain benchmark problem in 2D.

h	Element	Method	VF	L_0	tsche	δt	e_p	e_u	e_v
100	P1	ASGS	I	–	CN	0.16	0.057	0.081	0.081
100	P1	ASGS	I	–	BDF2	0.16	0.058	0.081	0.081
100	P2	ASGS	I	–	BDF2	0.16	0.058	0.081	0.081
100	P1	OSS	I	–	BDF2	0.16	0.058	0.081	0.081
100	P1	ASGS	I	–	BDF2	0.08	0.057	0.081	0.081
50	P1	ASGS	I	–	BDF2	0.08	0.056	0.081	0.081
100	P1	ASGS	II	100	BDF2	0.16	0.058	0.082	0.082
100	P1	ASGS	II	1000	BDF2	0.16	0.058	0.082	0.082
100	P1	ASGS	II	10	BDF2	0.16	0.058	0.082	0.082
100	P1	ASGS	III	100	BDF2	0.16	0.058	0.082	0.082

difference formulation with a node spacing of 100 per direction and a second order explicit time integration scheme is used in this reference, with a time step size equal to the critical time step needed for stability multiplied by 0.9.

5.2.3. Big/small domain benchmark problem in 3D

To test the NRBC in 3D, we solve a similar problem to the one in [18] extended to 3D. We choose the small domain as a cube of side 10 000 centered at the origin. The small domain is divided in $50 \times 50 \times 50$ Q1 elements ($h = 200$) with the NRBC applied on the whole boundary. The simulation time is $T = 24$, the time step size is taken as 0.16 and the time scheme used is BDF2. The equation coefficients μ_p and μ_u, as well as the initial condition, are chosen to be the same as before, in the 2D case. The only change is that the initial condition is in a sphere of radius R, so now r is computed as $r = \sqrt{x^2 + y^2 + z^2}$.

For comparison, a reference solution $p_{R,h}$ is obtained in a bigger domain, namely, a cube of side 20 000 with the region of interest in its center. The big domain is divided in $100 \times 100 \times 100$ Q1 elements and the boundary condition $p_{R,h} = 0$ is imposed. The error is computed as in the 2D version of the case with Eq. (53). Fig. 11 shows the contours of p in the plane $z = 0$ for the small domain at $t = 0$, $t = 8$ and $t = 16$, whereas Fig. 12 shows the contours of p in the plane $z = 0$ for the big domain at the same instants. A good qualitative agreement is observed.

Fig. 13 shows a cut at $y = z = 0$ for $0 \leqslant x \leqslant 5000$ of p_h and $p_{R,h}$ at $t = 8$, 16 and 24. Significant discrepancies are only observed at $t = 24$. However, they have small energy, as shown below.

The results obtained with our NRBC are presented in Table 10 for various mesh sizes (500, 250 and 200), polynomial order (Q1 and Q2), stabilization methods (ASGS and OSS), variational forms (I–III) and domain length scales (25, 250 and 2500). It can be seen that the error for p is around 7.9% and the error for $\boldsymbol{u}$ is around 8.6% for all cases.
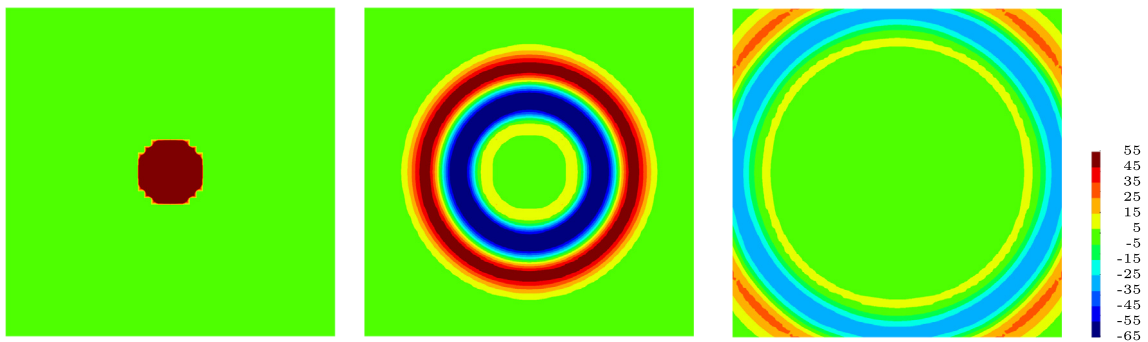

Fig. 11. Contours of p_h in the small domain for the big/small domain benchmark problem in 3D. From the left to the right: $t = 0$, 8 and 16 (ASGS method, VF I, $h = 200$, Q1 elements).
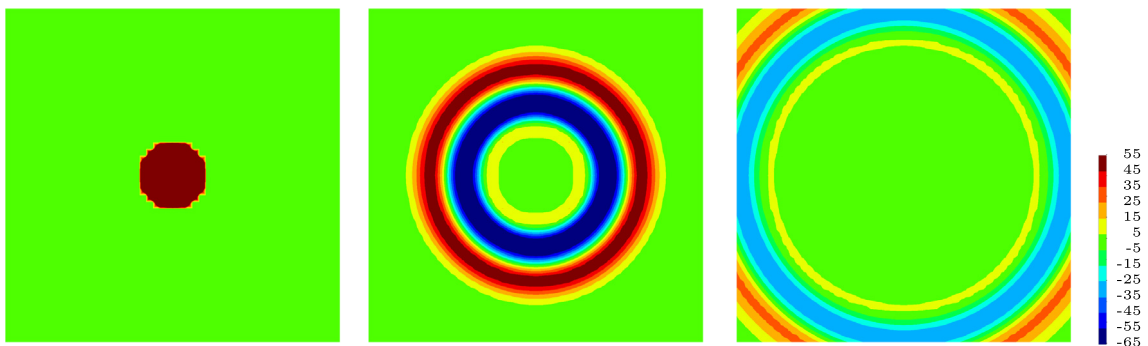

Fig. 12. Contours of $p_{R,h}$ in the big domain for the big/small domain benchmark problem in 3D. From the left to the right: $t = 0$, 8 and 16 (ASGS method, VF I, $h = 200$, Q1 elements).
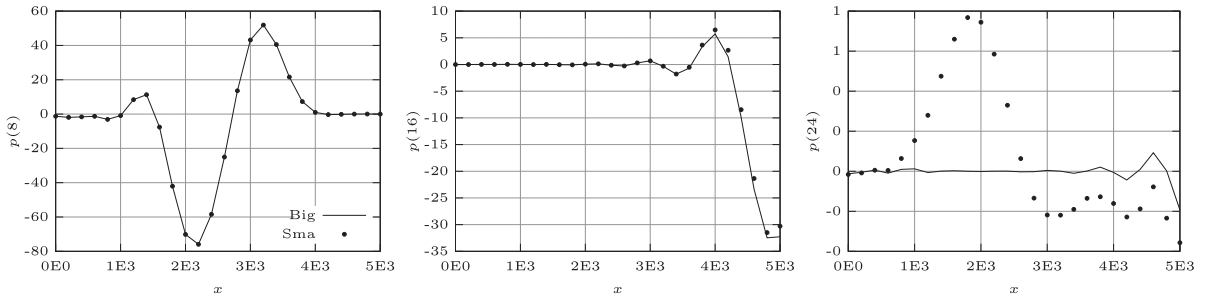
Fig. 13. Cut at $y = 0$ of p for the big/small domain benchmark problem in 3D (ASGS method, VF I, $h = 200$, Q1 elements). From the left to the right: $t = 8$, 16 and 24.

Table 10
Error of the NRBC for the big/small domain benchmark problem in 3D.

h	Element	Method	VF	L_0	e_p	e_u
500	Q1	ASGS	I	–	0.077	0.084
250	Q1	ASGS	I	–	0.078	0.085
200	Q1	ASGS	I	–	0.077	0.085
250	Q2	ASGS	I	–	0.081	0.090
250	Q1	OSS	I	–	0.078	0.086
250	Q1	ASGS	II	100	0.081	0.090
250	Q1	ASGS	III	100	0.081	0.090
250	Q1	ASGS	II	25	0.081	0.090
250	Q1	ASGS	II	2500	0.081	0.090

Fig. 14 shows the evolution in time of the energy E in the region of interest for the case with mesh size 250 m, the ASGS method, Q1 elements and VF I. It can be seen that the solution obtained with the NRBC behaves as the big domain solution.

5.2.4. Showcase problem with NRBC in 2D

An illustrative NRBC showcase appeared in [17] by Glowinski et al. Although it is not a benchmark of the NRBC, a plot of the evolution in time of the total energy of the system illustrates that the energy goes out of the region of interest and never enters again because the total energy decreases monotonically. The problem is defined in a square domain $\Omega = (-0.5, 0.5) \times (-0.5, 0.5)$, with $\mu_p = 1$ and $\mu_u = 1$. The simulation time is $T = 1$. The initial solution is $p(\boldsymbol{x}, 0) = 0$ and
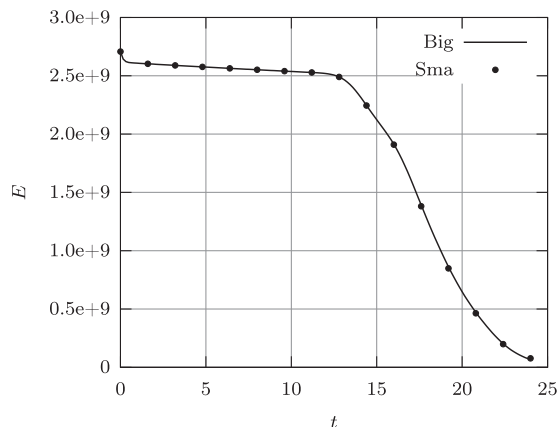
Fig. 14. Evolution of total energy E for the big/small domain benchmark problem in 3D.

$$\boldsymbol{u}(\boldsymbol{x},0) = \begin{cases} -\frac{4\pi}{r}\sin(2\pi r)\cos(2\pi r)\begin{bmatrix} x \\ y \end{bmatrix} & r \leqslant R, \\ \boldsymbol{0} & \text{otherwise} \end{cases}$$

with $r = \sqrt{x^2 + y^2}$, $R = 0.25$. In all the boundary the NRBC is applied. The problem is solved with a mesh size $h = 0.01$, a time step of $\delta t = 0.002$ and the time integration scheme is BDF2.

Additionally, we have defined a big domain to compare the results of the NRBC in the small domain. The big domain is taken as $\Omega = (-1.5, 1.5) \times (-1.5, 1.5)$. Fig. 15 shows the contours of $|\boldsymbol{u}_h|$ computed in the small domain at $t = 0$, $t = 0.3$ and $t = 0.6$. Fig. 16 shows the contours of $|\boldsymbol{u}_{R,h}|$, the solution computed in the big domain, at the same instants. It is observed that there is a certain distortion of the wave at $t = 0.6$ close to the boundary in the small domain case, which is not observed in the solution computed in the big domain.

The evolution of total energy inside the domain of interest is shown in Fig. 17. The agreement between the energy computed in both the big and the small domains is very good, indicating that the wave distortion close to the boundary of the solution computed in the small domain has low energy.

The error of the small domain with respect to the big domain in $L^\infty(\Upsilon, L^2(\Omega))$ norm for VF I, the ASGS method and P1 elements was 6.8% for p and 5.3% for $\boldsymbol{u}$.

5.2.5. Showcase problem with NRBL in 2D

A NRBL example appeared in [6] by Qi et al. It uses PML as NRBL. We solve the same example using our NRBC and compare the results. The domain is a hollow cylinder that extends from $r = 1$ to $r = 1 + H$, with $H = 1$. The mesh size is $h = 0.01$ in the radial direction and has 720 divisions in the circumferential direction. The coefficients of the equation are taken as $\mu_p = 1$ and $\mu_u = 1$. The simulation time is $T = 4$, the time step size is $\delta t = 0.005$ and the time integration algorithm is BDF2. The initial condition is zero for both p and $\boldsymbol{u}$. The boundary condition at $r = 1$ changes from a prescription in p to a prescription in $\gamma_n \boldsymbol{u}$, and is given by:
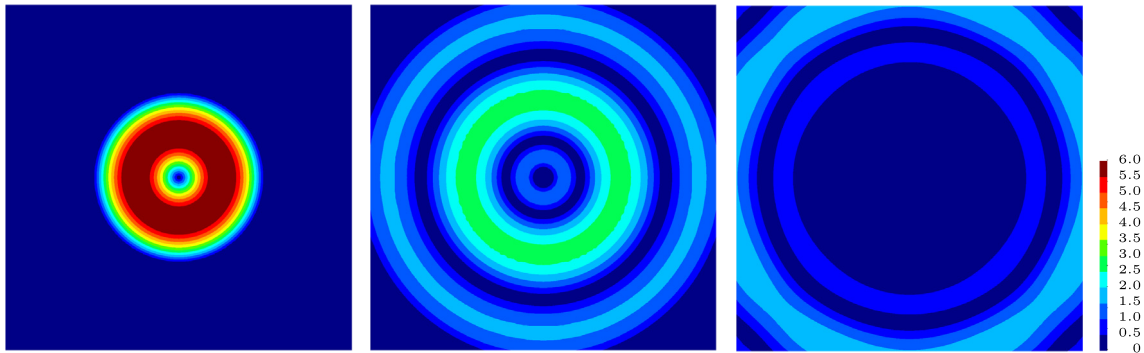

Fig. 15. Contours of $|\boldsymbol{u}_h|$ in the small domain for the showcase problem with NRBC. From the left to the right: $t = 0$, $t = 0.3$ and $t = 0.6$.
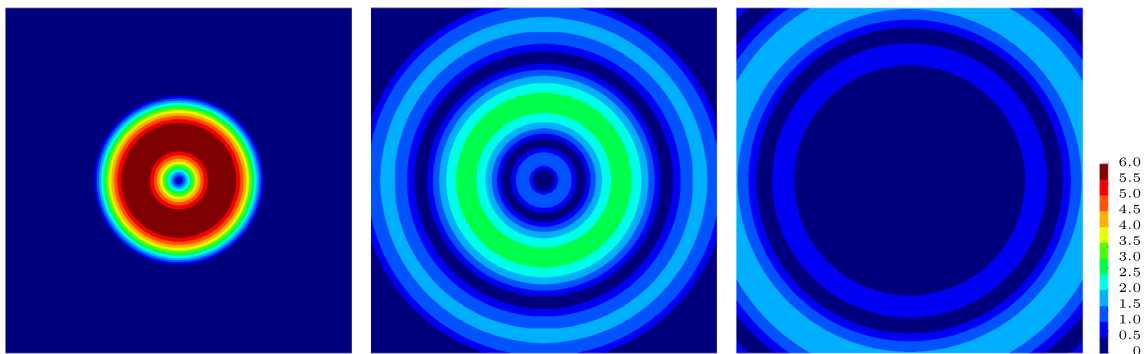

Fig. 16. Contours of $|\boldsymbol{u}_{R,h}|$ in the big domain for the showcase problem with NRBC. From the left to the right: $t = 0$, $t = 0.3$ and $t = 0.6$.
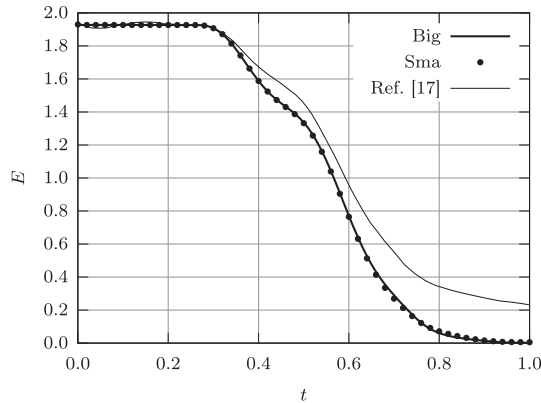
Fig. 17. Evolution of total energy E for the showcase problem with NRBC.

$$p = \cos(2\pi t) \quad 0 < t \leqslant 1, \ r = 1,$$
$$\gamma_n \boldsymbol{u} = 0 \qquad\quad 1 < t < 4, \ r = 1.$$

At $r = 1 + H$ the NRB is prescribed. In the case of [6], as a PML strategy is used, the domains extends from $r = 1 + H$ to $r = 1 + H + \delta$ to include the absorbing PML. The case with $\delta = 2$ from [6] was chosen as it is the one that provides less reflection according to their results. In Fig. 18 it is shown the evolution of p at $r = 1$ with our method and the comparison with the results obtained using PML by Qi and Geers [6].

In addition to the results presented in [6], we followed the big/small domain approach as in the previous examples, taking $1 < r < 2(1 + H)$ as the big domain. Fig. 19 shows the contours of p_h in the small domain at $t = 0,\ 0.5$ and 1.0, whereas Fig. 20 shows the contours of the solution computed in the big domain, $p_{R,h}$, at the same time instants.

Fig. 21 shows the energy evolution inside the domain of interest. As in the previous examples, the differences between the solutions in the small and the big domains have low energy.

The error of the small domain with NRBC respect to the big domain in $L^\infty(\Upsilon, L^2(\Omega))$ norm for VF I, the ASGS method and Q1 elements was 5.3% for p and 3.8% for $\boldsymbol{u}$.

In addition to the Big/Small domain analysis, we performed a Big/Medium/Small domain analysis. The idea is to compare the solutions in the medium and small domains with respect to the solution in the big domain. The medium domain was taken with $H = 1.83$ and the error in the medium domain with respect to the big domain in $L^\infty(\Upsilon, L^2(\Omega))$ norm for VF I, the ASGS method and Q1 elements was 3.4% for p and 2.3% for $\boldsymbol{u}$. The small domain corresponds to a location of the NRBC of $R = 2$, whereas the medium domain has $R = 2.83$. With the errors obtained we can infer that the error is proportional to $(1/R^2)^J$ with $J \approx 0.66$.
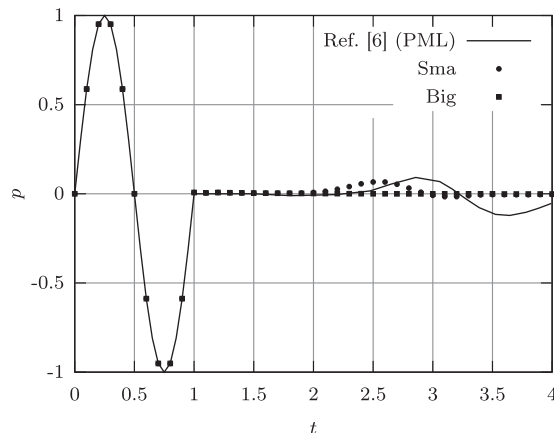

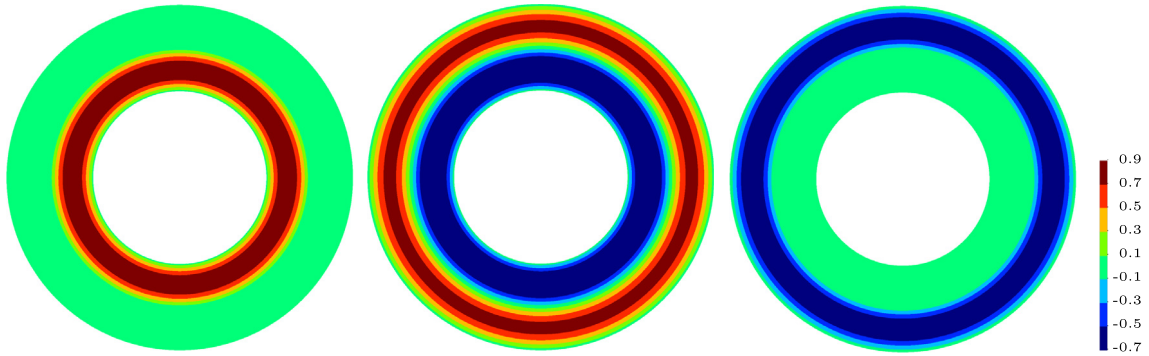Fig. 18. Evolution of p_h at $r = 1$ for the showcase problem with NRBL.

Fig. 19. Contours of p_h in the small domain for the showcase problem with NRBL. From the left to the right: $t = 0$, $t = 0.5$ and $t = 1.0$.
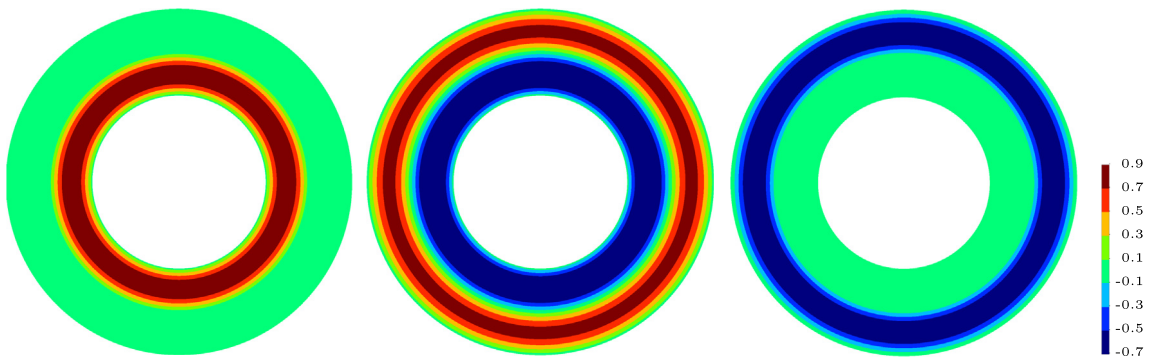

Fig. 20. Contours of $p_{R,h}$ in the big domain for the showcase problem with NRBL. From the left to the right: $t = 0$, $t = 0.5$ and $t = 1.0$.
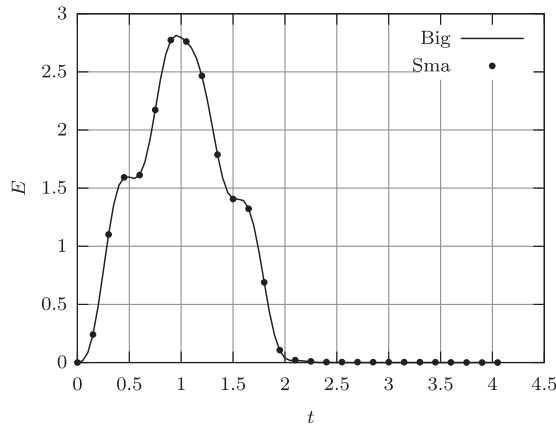

Fig. 21. Evolution of total energy E for the showcase problem with NRBL.

6. Conclusions

In this work, we have described a NRBC for the wave equation in mixed form in time domain. In particular, we have considered Sommerfeld-type artificial boundary conditions. The resulting system of equations has been stated in three different functional settings, based on the regularity required for the scalar and vector unknowns. The introduction of the NRBC terms require to increase the regularity of the functional setting for problems in bounded domains [39]. The extra regularity required is somehow small because the set of

functions in $H(\text{div}, \Omega)$ with normal trace in $L^2(\Gamma_o)$ is *close* to $H(\text{div}, \Omega)$, considering that $H^{\frac{1}{2}+\epsilon}(\Omega)$ has trace in $L^2(\Gamma)$ for any $\epsilon > 0$ and that $H^1(\Omega)$ has trace in $H^{\frac{1}{2}}(\Gamma)$.

We have presented two stabilized FE methods (ASGS and OSS) including the NRBC. Additionally, the stabilized methods can mimic the three variational forms of the problem, which require different regularity of the unknowns, via a proper design of the stabilization parameters. Stability and convergence results have been presented for these stabilized FE formulations. The NRBC does not affect previous results proved in [39] for Dirichlet-type boundary conditions, although it requires extra regularity on the boundary for the vector unknown in variational forms I and II. We normally use the stabilized FE formulations for equal interpolation of the unknowns, but the analysis is not restricted to that and allows any continuous interpolation pair.

Numerical experiments have been carried out to check the accuracy of the methods and the results obtained are in agreement with the accuracy predicted theoretically. Benchmark problems have been solved using the NRBCs proposed and good results have been obtained when compared with other NRBCs or NRBLs. The main practical advantage of the NRBC described over other NRBCs is its simplicity and the fact that no non-linear or iterative methods are required. Further, for NRBC schemes, the truncated domain does not need to be extended with an absorbing layer. Additionally, when compared to PML techniques, it avoids extra degrees of freedom per node and avoids the solution of other governing equations in the absorbing layer.

Acknowledgments

References

[1] D. Givoli, High-order local non-reflecting boundary conditions: a review, Wave Motion 39 (2004) 319–326.
[2] S.V. Tsynkov, Numerical solution of problems on unbounded domains. A review, Appl. Numer. Math. 27 (1998) 465–532.
[3] D. Appelö, G. Kreiss, Application of a perfectly matched layer to the nonlinear wave equation, Wave Motion 44 (2007) 531–548.
[4] J. Diaz, P. Joly, A time domain analysis of PML models in acoustics, Comput. Methods Appl. Mech. Eng. 195 (2006) 3820–3853.
[5] S. Richards, X. Zhang, X. Chen, P. Nelson, The evaluation of non-reflecting boundary conditions for duct acoustic computation, J. Sound Vib. 270 (2004) 539–557.
[6] Q. Qi, T.L. Geers, Evaluation of the perfectly matched layer for computational acoustics, J. Comput. Phys. 139 (1998) 166–183.
[7] Y. Zhou, Z.J. Wang, Absorbing boundary conditions for the Euler and Navier–Stokes equations with the spectral difference method, J. Comput. Phys. 229 (2010) 8733–8749.
[8] F.Q. Hu, A perfectly matched layer absorbing boundary condition for linearized Euler equations with a non-uniform mean flow, J. Comput. Phys. 208 (2005) 469–492.
[9] J.S. Hesthaven, On the analysis and construction of perfectly matched layers for the linearized Euler equations, J. Comput. Phys. 142 (1998) 129–147.
[10] J.-P. Berenger, A perfectly matched layer for the absorption of electromagnetic waves, J. Comput. Phys. 114 (1994) 185–200.
[11] D. Givoli, Computational absorbing boundaries, in: S. Marburg, B. Nolte (Eds.), Computational Acoustics of Noise Propagation in Fluids, vol. 31, Springer, Berlin, Heidelberg, 2008, pp. 145–166.
[12] A. Sommerfeld, Partial Differential Equations in Physics, Elsevier, 1949.
[13] M. Zhao, X. Du, J. Liu, H. Liu, Explicit finite element artificial boundary scheme for transient scalar waves in two-dimensional unbounded waveguide, Int. J. Numer. Methods Eng. 87 (2011) 1074–1104.
[14] E. Bécache, D. Givoli, T. Hagstrom, High-order absorbing boundary conditions for anisotropic and convective wave equations, J. Comput. Phys. 229 (2010) 1099–1129.
[15] J. Diaz, P. Joly, An analysis of higher order boundary conditions for the wave equation, SIAM J. Appl. Math. 65 (2005) 1547–1575.
[16] D. Givoli, B. Neta, High-order non-reflecting boundary scheme for time-dependent waves, J. Comput. Phys. 186 (2003) 24–46.
[17] R. Glowinski, S. Lapin, Solution of a wave equation by a mixed finite element – fictitious domain method, Comput. Methods Appl. Math. 4 (2004) 431–444.
[18] J.R. Dea, F.X. Giraldo, B. Neta, High-order non-reflecting boundary conditions for the linearized 2-D Euler equations: no mean flow case, Wave Motion 46 (2009) 210–220.
[19] B. Engquist, A. Majda, Absorbing boundary conditions for numerical simulation of waves, Math. Comput. 31 (1977) 629–651.

[20] A. Bayliss, E. Turkel, Radiation boundary conditions for wave-like equations, Commun. Pure Appl. Math. 33 (1980) 707–725.
[21] R.L. Higdon, Numerical absorbing boundary conditions for the wave equation, Math. Comput. 49 (1987) 65–90.
[22] J.B. Keller, D. Givoli, Exact non-reflecting boundary conditions, J. Comput. Phys. 82 (1989) 172–192.
[23] V. Ryaben'Kii, S.V. Tsynkov, Artificial boundary conditions for the numerical solution of external viscous flow problems, SIAM Journal Numer. Anal. 32 (1995) 1355–1389.
[24] F. Collino, High order absorbing boundary conditions for wave propagation models: straight line boundary and corner cases, in: Second International Conference on Mathematical and Numerical Aspects of Wave Propagation, SIAM, 1993, pp. 161–171.
[25] M. Grote, J. Keller, Exact nonreflecting boundary conditions for the time dependent wave equation, SIAM J. Appl. Math. 55 (1995) 280–297.
[26] C.W. Rowley, T. Colonius, Discretely nonreflecting boundary conditions for linear hyperbolic systems, J. Comput. Phys. 157 (2000) 500–538.
[27] M.N. Guddati, J.L. Tassoulas, Continued-fraction absorbing boundary conditions for the wave equation, J. Comput. Acoust. 08 (2000) 139–156.
[28] T. Hagstrom, T. Warburton, A new auxiliary variable formulation of high-order local radiation boundary conditions: corner compatibility conditions and extensions to first-order systems, Wave Motion 39 (2004) 327–338.
[29] F. Brezzi, M. Fortin, Mixed and Hybrid Finite Element Methods, Springer Verlag New York, Inc., New York, NY, USA, 1991.
[30] D. Arnold, F. Brezzi, M. Fortin, A stable finite element for the Stokes equations, Calcolo 21 (1984) 337–344.
[31] F. Brezzi, J. Douglas Jr., L.D. Marini, Two families of mixed finite elements for second order elliptic problems, Numer. Math. 47 (1985) 217–235.
[32] J.-C. Nédélec, A new family of mixed finite elements in $\mathbb{R}^3$, Numer. Math. 50 (1986) 57–81.
[33] T. Arbogast, D. Brunson, A computational method for approximating a Darcy–Stokes system governing a vuggy porous medium, Comput. Geosci. 11 (2007) 207–218.
[34] K.-A. Mardal, X.-C. Tai, R. Winther, A robust finite element method for Darcy–Stokes flow, SIAM J. Numer. Anal. 40 (2002) 1605–1631.
[35] E. Bécache, P. Joly, C. Tsogka, An analysis of new mixed finite elements for the approximation of wave propagation problems, SIAM J. Numer. Anal. 37 (2000) 1053–1084.
[36] E. Bécache, P. Joly, C. Tsogka, A new family of mixed finite elements for the linear elastodynamic problem, SIAM J. Numer. Anal. 39 (2002) 2109–2132.
[37] C. Makridakis, On mixed finite element methods for linear elastodynamics, Numer. Math. 61 (1992) 235–260.
[38] R. Codina, Finite element approximation of the hyperbolic wave equation in mixed form, Comput. Methods Appl. Mech. Eng. 197 (2008) 1305–1322.
[39] S. Badia, R. Codina, H. Espinoza, Stability, convergence and accuracy of stabilized finite element methods for the wave equation in mixed form (submitted for publication).
[40] P. Monk, Finite Element Methods for Maxwell's Equations, Oxford University Press, 2003.
[41] R. Codina, Analysis of a stabilized finite element approximation of the Oseen equations using orthogonal subscales, Appl. Numer. Math. 58 (2008) 264–283.
[42] T.J. Hughes, Multiscale phenomena: Green's functions, the Dirichlet-to-Neumann formulation, subgrid scale models, bubbles and the origins of stabilized methods, Comput. Methods Appl. Mech. Eng. 127 (1995) 387–401.
[43] T.J. Hughes, G.R. Feijoo, L. Mazzei, J.-B. Quincy, The variational multiscale method – a paradigm for computational mechanics, Comput. Methods Appl. Mech. Eng. 166 (1998) 3–24.
[44] R. Codina, Stabilization of incompressibility and convection through orthogonal sub-scales in finite element methods, Comput. Methods Appl. Mech. Eng. 190 (2000) 1579–1599.
[45] R. Codina, Stabilized finite element approximation of transient incompressible flows using orthogonal subscales, Comput. Methods Appl. Mech. Eng. 191 (2002) 4295–4321.
[46] S. Badia, R. Codina, Unified stabilized finite element formulations for the Stokes and the Darcy problems, SIAM J. Numer. Anal. 47 (2009) 1971–2000.
[47] S. Badia, R. Codina, Analysis of a stabilized finite element approximation of the transient convection-diffusion equation using an ALE framework, SIAM J. Numer. Anal. 44 (2006) 2159–2197.
[48] J.C. Hardin, J.R. Ristorcelli, C.K.W. Tam (Eds.), ICASE/LaRC Workshop on Benchmark Problems in Computational Aeroacoustics (CAA), National Aeronautics and Space Administration, Langley Research Center, 1995.
[49] M.D. Dahl (Ed.), Fourth Computational Aeroacoustics (CAA) Workshop on Benchmark Problems, NASA, Glenn Research Center, 2004.